

TESTING THE UNIFICATION MODEL FOR AGN IN THE INFRARED: ARE THE OBSCURING TORI OF TYPE 1 AND 2 SEYFERTS DIFFERENT?

C. RAMOS ALMEIDA¹, N. A. LEVENSON², A. ALONSO-HERRERO³, A. ASENSIO RAMOS^{4,5}, J. M. RODRÍGUEZ ESPINOSA^{4,5}, A. M. PÉREZ GARCÍA^{4,5}, C. PACKHAM⁶, R. MASON⁷, J. T. RADOMSKI², AND T. DÍAZ-SANTOS⁸

Draft version January 19, 2011

ABSTRACT

We present new mid-infrared (MIR) imaging data for three Type-1 Seyfert galaxies obtained with T-ReCS on the Gemini-South Telescope at subarcsecond resolution. Our aim is to enlarge the sample studied in a previous work to compare the properties of Type-1 and Type-2 Seyfert tori using clumpy torus models and a Bayesian approach to fit the infrared nuclear spectral energy distributions (SEDs). Thus, the sample considered here comprises 7 Type-1, 11 Type-2, and 3 intermediate-type Seyferts. The unresolved IR emission of the Seyfert 1 galaxies can be reproduced by a combination of dust heated by the central engine and direct AGN emission, while for the Seyfert 2 nuclei only dust emission is considered. These dusty tori have physical sizes smaller than 6 pc radius, as derived from our fits. Unification schemes of AGN account for a variety of observational differences in terms of viewing geometry. However, we find evidence that strong unification may not hold, and that the immediate dusty surroundings of Type-1 and Type-2 Seyfert nuclei are intrinsically different. The Type-2 tori studied here are broader, have more clumps, and these clumps have lower optical depths than those of Type-1 tori. The larger the covering factor of the torus, the smaller the probability of having direct view of the AGN, and vice-versa. In our sample, Seyfert 2 tori have larger covering factors ($C_T=0.95\pm0.02$) and smaller escape probabilities ($P_{esc}=0.05\pm^{0.08}_{0.03}\%$) than those of Seyfert 1 ($C_T=0.5\pm0.1$; $P_{esc}=18\pm3\%$). All the previous differences are significant according to the Kullback-Leibler divergence. Thus, on the basis of the results presented here, the classification of a Seyfert galaxy as a Type-1 or Type-2 depends more on the intrinsic properties of the torus rather than on its mere inclination towards us, in contradiction with the simplest unification model.

Subject headings: galaxies: active – galaxies: nuclei – galaxies: Seyfert – infrared: galaxies

1. INTRODUCTION

Observational evidence in the X-rays and the MIR indicates that the strong AGN continuum source must be absorbed by obscuring material over a wide solid angle (see e.g., Antonucci & Miller 1985; Maiolino et al. 1998; Risaliti et al. 2002). According to observed spectra of different AGN types, the obscuring structure has to block the emission of the subparsec-scale Broad-Line Region (BLR) where the broad lines are produced, but not that of the kiloparsec-scale Narrow-Line Region (NLR).

The unified model for active galaxies (Antonucci 1993; Urry & Padovani 1995) is based on the existence of a dusty toroidal structure surrounding the central region of AGN. This toroidal geometry explains the biconical shapes observed in Hubble Space Telescope (HST) imaging of several AGNs (Tadhunter & Tsvetanov 1989; Malkan et al. 1998; Tadhunter et al. 1999) and also the polarimetric observations (Antonucci & Miller 1985; Packham et al. 1997). Thus, considering this geometry

of the obscuring material, the central engines of Type-1 AGN can be seen directly, resulting in typical spectra with both narrow and broad emission lines, whereas in Type-2 AGN the BLR is obscured.

Pioneering work in modelling the dusty torus (Pier & Krolik 1992, 1993; Granato & Danese 1994; Efstathiou & Rowan-Robinson 1995; Granato et al. 1997; Siebenmorgen et al. 2004) assumed a uniform dust density distribution to simplify the modelling, although from the start, Krolik & Begelman (1988) realized that smooth dust distributions cannot survive within the AGN vicinity. They proposed instead that the material in the torus must be distributed in a clumpy structure, in order to prevent the dust grains from being destroyed by the hot surrounding gas.

The IR range (and particularly the MIR) is key to set constraints on the torus models, since the reprocessed radiation from the dust in the torus is re-emitted in this range. However, in comparing the predictions of any torus model with observations, its small-scale emission must be isolated. High angular resolution is then essential to separate torus emission from stellar emission and star-heated dust in the near-IR (NIR) and MIR, respectively. Indeed, starlight dominates the nuclear NIR emission of Seyfert 2 galaxies when using large aperture data (see e.g., Alonso-Herrero et al. 1996) and still has a significant contribution for Seyfert 1 galaxies (Kotilainen et al. 1992). Similar contamination problems can be present in the MIR with the star-heated dust and dust in the ionization cones (Alonso-Herrero et al. 2006; Mason et al. 2006).

¹ University of Sheffield, Department of Physics & Astronomy, S3 7RH, UK; C.Ramos@sheffield.ac.es

² Gemini Observatory, Casilla 603, La Serena, Chile.

³ Centro de Astrobiología, INTA-CSIC, E-28850, Madrid, Spain.

⁴ Instituto de Astrofísica de Canarias (IAC), Tenerife, Spain

⁵ Departamento de Astrofísica, Universidad de La Laguna, Tenerife, Spain

⁶ Astronomy Department, University of Florida, Gainesville, FL 32611-2055.

⁷ Gemini Observatory, Northern Operations Center, 670 North Aöhoku Place, Hilo, HI 96720.

⁸ Department of Physics, University of Crete, GR-71003, Heraklion, Greece.

Another controversial issue about the torus structure is its typical dimensions. Pier & Krolik (1993) and Granato & Danese (1994) reproduced the infrared observations of nearby Seyfert galaxies with ~ 100 pc scale tori. However, hard X-ray observations showed that about half of nearby Type-2 Seyferts are Compton-thick (i.e., they are obscured by a column density higher than 10^{24} cm^{-2} ; Risaliti et al. 1999). For these highly obscured sources the torus dimensions are expected to be of a few parsecs, because otherwise the dynamical mass of the obscuring material would be too large to be realistic (Risaliti et al. 1999). In addition, recent ground-based MIR observations of nearby Seyferts reveal that the torus size is likely restricted to a few parsecs. Packham et al. (2005) and Radomski et al. (2008) established upper limits of 2 and 1.6 pc for the outer radii of the Circinus galaxy and Centaurus A tori, respectively. Besides, interferometric observations obtained with the MIR Interferometric Instrument (MIDI) at the Very Large Telescope Interferometer (VLTI) of Circinus, NGC 1068, and Centaurus A suggest a scenario where the torus emission would only extend out to $R = 1$ pc (Tristram et al. 2007), $R = 1.7 - 2$ pc (Jaffe et al. 2004; Raban et al. 2009), and $R = 0.3$ pc (Meisenheimer et al. 2007), respectively.

In order to solve the discrepancies between observations and previous models, an intensive search for an alternative torus geometry has been carried out in the last decade. The first results of radiative transfer calculations of a clumpy rather than a smooth medium were reported by Nenkova et al. (2002) and Elitzur & Shlosman (2006), and further work was done by Dullemond & van Bemmel (2005). The clumpy dusty torus models (Nenkova et al. 2002, 2008a,b; Höning et al. 2006; Schartmann et al. 2008) propose that the dust is distributed in clumps, instead of homogeneously filling the torus volume. These models are making significant progress in accounting for the MIR emission of AGNs (Mason et al. 2006, 2009; Mor et al. 2009; Horst et al. 2008, 2009; Nikutta et al. 2009; Ramos Almeida et al. 2009a; Höning et al. 2010).

In our previous work (Ramos Almeida et al. 2009a; hereafter RA09), we constructed subarcsecond resolution IR SEDs for eighteen Seyfert galaxies, mostly Type-2 Seyferts. From the comparison between our high angular resolution MIR fluxes and large aperture data, such as those from ISO, IRAS, or Spitzer, we confirmed that the former provide a spectral shape that is substantially different from that of the large aperture data (Rodríguez Espinosa & Pérez García 1997). Since our nuclear measurements allowed us to better characterize the torus emission, we modelled our SEDs with clumpy torus models. In general, we found that Type-2 views are more inclined than those of Type-1s, and more importantly, we derive larger covering factors for the Type-2 tori (i.e., more clumps and wider torus angular distributions). This would imply that the observed differences between Type-1 and Type-2 AGN would not be due to orientation effects only, but to intrinsic differences in their tori. However, due to the limited size of the sample analyzed by RA09, and in particular of Type-1 Seyferts compared with Type-2s, our aim is to enlarge the sample studied in the previous work with new Seyfert 1 infrared data to compare the properties of Type-1 and Type-2 Seyfert tori.

In this work, we report new subarcsecond MIR imaging

data for the 3 nearby Type-1 Seyfert galaxies NGC 7469, NGC 6221, and NGC 6814, for which we estimate unresolved nuclear MIR fluxes. We enlarge the sample by including the galaxies NGC 1097, NGC 1566, NGC 3227, and NGC 4151, which have similar MIR data, and we compile NIR nuclear fluxes from the literature of similar resolution to construct nuclear SEDs for all the galaxies. We fit these SEDs with clumpy torus models which we interpolate from the Nenkova et al. (2008a,b) database, and compare them with the larger sample studied by RA09. Table 1 summarizes key observational properties of the sources in the sample. Section 2 describes the observations, data reduction, and compilation of NIR and MIR fluxes. Sections 3 and 4 present the main observational results, and in §5 we report the modelling results. We discuss differences between Type-1 and Type-2 Seyferts and draw conclusions about the clumpy torus models and AGN obscuration in general in §6. Finally, Section 7 summarizes the main conclusions of this work.

2. OBSERVATIONS AND DATA REDUCTION

2.1. MIR Imaging Observations

In order to enlarge the sample of 18 Seyfert galaxies presented in RA09, which comprises 12 Seyfert 2 (Sy2), two Seyfert 1.9 (Sy1.9), one Seyfert 1.8 (Sy1.8), two Seyfert 1.5 (Sy1.5), and one Seyfert 1 galaxy (Sy1), we obtained new subarcsecond MIR observations of the Type-1 Seyferts NGC 6221, NGC 6814, and NGC 7469 (see Table 1).

The observations were performed with the MIR camera/spectrograph T-ReCS (Thermal-Region Camera Spectrograph; Telesco et al. 1998) on the Gemini-South telescope during the Summer of 2009. T-ReCS uses a Raytheon 320x240 pixel Si:As IBC array, providing a plate scale of $0.089'' \text{ pixel}^{-1}$, corresponding to a FOV of $28.5'' \times 21.4''$. The filters employed for the observations were the narrow Si-2 filter ($\lambda_c=8.74 \mu\text{m}$, $\Delta\lambda=0.78 \mu\text{m}$, 50% cut-on/off) and the broad Qa filter ($\lambda_c=18.3 \mu\text{m}$, $\Delta\lambda=1.5 \mu\text{m}$, 50% cut-on/off). The resolutions obtained were $0.3''$ at $8.7 \mu\text{m}$ and $0.5''$ at $18.3 \mu\text{m}$, as measured from the observed Point Spread Function (PSF) stars. A summary of the observations is reported in Table 2.

The standard chopping-nodding technique was used to remove the time-variable sky background, the telescope thermal emission, and the so-called 1/f detector noise. The chopping throw was $15''$, and the telescope was nodded $15''$ in the direction of the chop every 45 s. The difference for each chopped pair for each given nodding set was calculated, and the nod sets were then differenced and combined until a single image was created. The data were reduced using in-house-developed IDL routines.

Observations of flux standard stars were made for the flux calibration of each galaxy through the same filters. The uncertainties in the flux calibration are typically $\sim 5\text{--}10\%$ at $8.7 \mu\text{m}$ and $\sim 15\text{--}20\%$ at $18.3 \mu\text{m}$. PSF star observations were also made immediately prior to or after each galaxy observation to accurately sample the image quality. These images were employed to determine the unresolved (i.e., nuclear) component of each galaxy. The PSF star, scaled to the peak of the galaxy emission, represents the maximum contribution of the unresolved source (100%), where we integrate flux within an aperture of $2''$. The residual of the total emission minus the scaled PSF represents the host galaxy contribution,

TABLE 1
BASIC GALAXY DATA

Galaxy	Seyfert Type	Ref.	z	Distance (Mpc)	Scale (pc arcsec $^{-1}$)	Ref.
NGC 1097	Sy1 [†]	A1	0.0042	19	92	B1
NGC 1566	Sy1	A2	0.0050	20	97	B2
NGC 6221	Sy1	A3	0.0050	18	87	B3
NGC 6814	HII/Sy1.5	A4	0.0052	21	102	B4
NGC 7469	Sy1	A5	0.0163	65	315	B5
NGC 3227	Sy1.5	A6	0.0039	17	82	B6
NGC 4151	Sy1.5	A7	0.0033	13	64	B7

REFERENCES. — (A1) Storchi-Bergmann et al. (1997); (A2) Kriss et al. (1990); (A3) Levenson et al. (2001); (A4) Véron-Cetty & Véron (2006); (A5) Osterbrock & Martel (1993); (A6) Rubin & Ford (1968); (A7) Ayani & Maelha (1991); (B1) Willick et al. (1997); (B2) Sandage & Bedke (1994); (B3) Koribalski & Dickey (2004); (B4) Liszt & Dickey (1995); (B5) Heckman et al. (1986); (B6) Garcia (1993); (B7) Radomski et al. (2003).

NOTE. — Classification and distance are taken from the literature (references below) and spectroscopic redshift from the NASA/IPAC Extragalactic Database (NED).

[†]Originally classified as a LINER by Keel (1983) and Phillips et al. (1984).

TABLE 2
SUMMARY OF MIR OBSERVATIONS

Galaxy	Filters	Observation epoch	On-Source N band	Time (s) Q band	PSF FWHM N band	PSF FWHM Q band
NGC 1097	Si-5, Qa	Sep 2005	456	912	0.41''	0.52''
NGC 1566	Si-2, Qa	Sep 2005	152	304	0.30''	0.53''
NGC 6221	Si-2, Qa	Aug 2009	145	203	0.32''	0.55''
NGC 6814	Si-2, Qa	Aug 2009	145	203	0.28''	0.53''
NGC 7469	Si-2, Qa	Sep 2009	145	203	0.31''	0.55''
NGC 3227	N'	Apr 2006	300	...	0.39''	...
NGC 4151	N, IHW18	May 2001	360	480	0.53''	0.58''

NOTE. — Images were obtained in the 8.74 μm (Si-2, $\Delta\lambda = 0.78 \mu\text{m}$ at 50% cut-on/off), 11.66 μm (Si-5, $\Delta\lambda = 1.13 \mu\text{m}$), and 18.30 μm (Qa, $\Delta\lambda = 1.5 \mu\text{m}$) T-ReCS filters. NGC 3227 was observed in the 11.29 μm (N', $\Delta\lambda = 2.4 \mu\text{m}$) Michelle/Gemini-North filter, and NGC 4151 in the 10.75 μm (N, $\Delta\lambda = 5.2 \mu\text{m}$) and 18.17 μm (IHW18, $\Delta\lambda = 1.7 \mu\text{m}$) OSCIR/Gemini-North filters.

which is analyzed in Section 3. We require a flat profile in the residual for a realistic galaxy profile over the central pixels. Therefore, we reduce the scale of the PSF from matching the peak of the galaxy emission (100%), when necessary, to obtain the unresolved fluxes reported in Table 3. They include corresponding aperture corrections to take into account possible flux losses when integrating the scaled PSF flux in the 2'' aperture.

Figure 1 shows an example of PSF subtraction at various levels (in contours) for NGC 7469 in the Si-2 T-ReCS filter, following Radomski et al. (2002, 2003). The residual profiles from the different scales demonstrate the best-fitting result. The uncertainty in the unresolved fluxes determination from PSF subtraction is \sim 10–15%. Thus, we estimated the errors in the flux densities reported in Table 3 by adding quadratically the flux calibration and PSF subtraction uncertainties, resulting in \sim 15% at 8.7 μm and \sim 25% at 18.3 μm .

2.2. Compilation of NIR and MIR High Spatial Resolution Data

In addition to the new T-ReCS observations described in Section 2.1, we include here two more Sy1 galaxies with already published T-ReCS data: NGC 1097 and

TABLE 3
UNRESOLVED MIR FLUXES

Galaxy	Level of PSF subtraction N band	Level of PSF subtraction Qa band	Flux Density (mJy) N band	Flux Density (mJy) Qa band
NGC 1097	80%	20%	23	55
NGC 1566 ^a	100%	100%	29	117
NGC 6221	80%	30%	48	314
NGC 6814	100%	40%	53	159
NGC 7469	85%	100%	174	1354
NGC 3227	100%	...	401	...
NGC 4151	90%	100%	1320	3200

NOTE. — The percentages of PSF subtraction level are reported in the employed filters (listed in Table 2). Errors in flux densities are dominated in general by uncertainties in the flux calibration and PSF subtraction (\sim 15% at N band and \sim 25% at Qa band). Fluxes include aperture corrections.

^aMIR fluxes for NGC 1566 are from aperture photometry using 0.45'' aperture radii (RA09).

NGC 1566⁹. We reduced the images presented in Mason et al. (2007) for NGC 1097 and obtained unresolved

⁹ NGC 1097 and NGC 1566 were not included in the analysis of the SEDs presented in RA09 because of the lack of high angular resolution NIR fluxes for them at the time of publication.

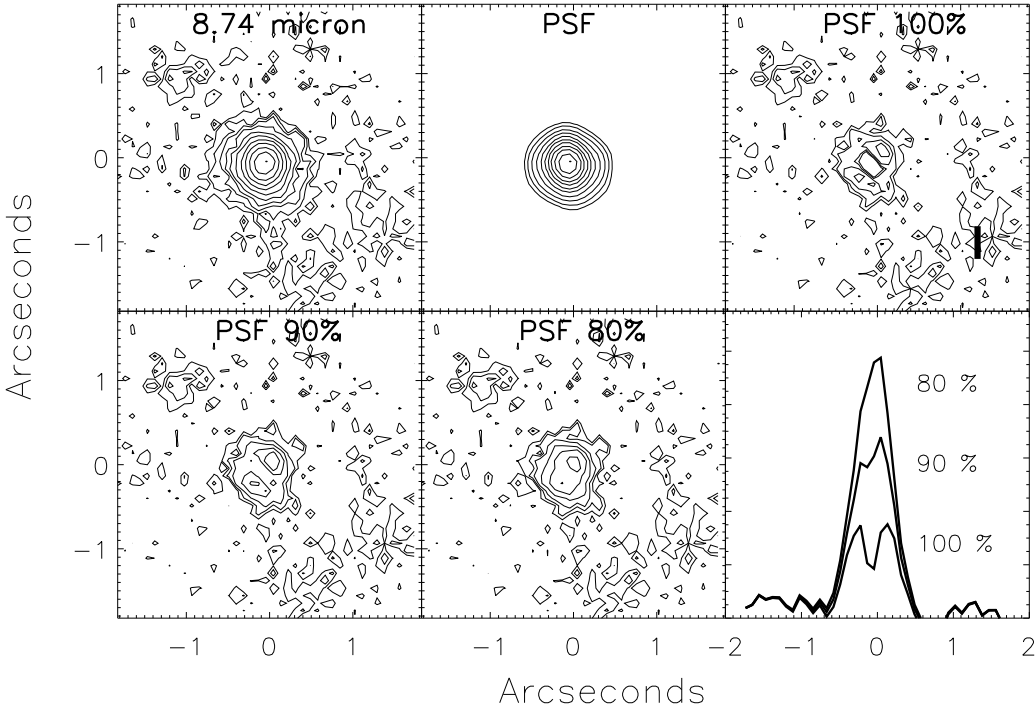


FIG. 1.— $8.74 \mu\text{m}$ contour plots of NGC 7469 at the 3σ level, the PSF star, and scaled subtraction of the PSF for this galaxy at various levels (100%, 90%, and 80%). The residuals of the subtraction in the lower right panel show the host galaxy profile.

MIR fluxes by performing the same technique explained in Section 2.1 (see Table 3). For NGC 1566 we compiled the MIR nuclear fluxes reported RA09. Both galaxies were observed in September 2005 with T-ReCS: NGC 1566 in the Si-2 and Qa filters, and NGC 1097 in the Si-5 ($\lambda_c=11.66 \mu\text{m}$, $\Delta\lambda=1.13 \mu\text{m}$, 50% cut-on/off) and Qa filters (see Table 2). The resolutions of the images are $0.3''$ at $8.7 \mu\text{m}$, $\sim 0.4''$ at $11.66 \mu\text{m}$, and $0.5''$ at $18.3 \mu\text{m}$.

NIR subarcsecond resolution nuclear fluxes compiled from the literature are reported in Table 4. For NGC 1097, NGC 1566, and NGC 7469, Prieto et al. (2010) reported diffraction-limited and near-diffraction-limited adaptive optics NACO/VLT fluxes. The three galaxies are unresolved in the NIR down to the highest resolution achieved (FWHM $\sim 0.15''$ for NGC 1097 in the L'-band, $\sim 0.12''$ for NGC 1566 in the K-band, and $\sim 0.08''$ for NGC 7469 in the H-band).

For NGC 7469, Prieto et al. (2010) reported NACO J-, H-, and K-band nuclear fluxes obtained from observations in Nov 2002, as well as in the L' and NB-4.05 μm filters, observed in this case in Dec 2005. First, we discarded the narrow-band filter, since it is designed to collect the Br α emission, which in the case of this galaxy is important (as inferred from the Br α line detected with NIR spectroscopy; Genzel et al. 1995; Hicks & Malkan 2008). The L'-band filter also contains Br α , which is very likely compromising the flux measurement, since the L' and NB-4.05 fluxes do not match the SED shape of the remaining J, H, K, Si-2 and Qa data. Indeed, Prieto et al. (2010) also reported a NICMOS/HST flux measurement in the filter F187N, obtained in 2007. This data point lies in between the NACO H and K measurements in wavelength and flux, which gives us extra-confidence

in the reliability of the NACO J, H, and K measurements. Considering all the previous, we finally decided to consider the NACO L'-band flux as an upper limit¹⁰.

For NGC 6221 and NGC 6814, which do not have any published subarcsecond resolution NIR data, we retrieved broad-band images from the Hubble Legacy Archive¹¹ obtained with NICMOS on the HST. The two galaxies were observed in the F160W filter, using the NIC2 camera, as part of the program 7330 (PI: Mulchaey, J.). The typical FWHM for an unresolved PSF is $\sim 0.13''$ using the F160W filter with NIC2. Details of the observations can be found in Scoville et al. (2000) and Regan & Mulchaey (1999). For the analysis, we first separated the nuclear emission from the underlying host galaxy emission. We then applied the two-dimensional image decomposition GALFIT program (Peng et al. 2002) to fit and subtract the unresolved component (PSF). PSF models were created using the Tiny-Tim software package, which includes the optics of HST plus the specifics of the camera and filter system (Krist 1993). We checked that no prominent emission lines are included in the wavelength range covered by the filter F160W. The resulting unresolved NIR fluxes for NGC 6221 and NGC 6814 are reported in Table 4.

We finally include the Sy1.5 galaxies NGC 3227 and NGC 4151 in this study, which were also part of the RA09 sample. The MIR nuclear fluxes are the same reported in the latter work (see description of the observa-

¹⁰ The nucleus of NGC 7469 had undergone different periods of activity, including a maximum in the optical happening in the period 1996 to 2000, followed by a relaxation epoch in the following years (Prieto et al. 2010). For this reason, here we only consider data obtained from 2002.

¹¹ <http://archive.stsci.edu/>

tions in Section 2.1 in RA09), whereas the NIR fluxes have been updated (see Table 4).

Using the NIR nuclear fluxes reported in Table 4 in combination with our MIR unresolved measurements (Table 3) we construct AGN-dominated SEDs for the five Sy1 galaxies.

3. THE MIR EXTENDED EMISSION OF NGC 7469 AND NGC 6221

Our new MIR imaging data reveal complex extended emission for NGC 7469 and NGC 6221, which is known to be intense and associated with emitting-dust heated by star formation. On the other hand, NGC 6814 lacks of any extended emission. In this section we present the MIR images of NGC 7469 and NGC 6221, and compare them with published data in different wavelength ranges.

3.1. NGC 7469

The most spectacular morphological feature of this Sy1 galaxy is a circumnuclear ring of powerful starbursts of ~ 1.6 kpc diameter, which is deeply embedded in a large cloud of molecular gas and dust. This ring contains several super star clusters and regions of star formation and it accounts for two-thirds of the galaxy bolometric luminosity (Genzel et al. 1995). The star-forming ring has been the subject of study of several works in different wavelengths (see Díaz-Santos et al. 2007, hereafter DS07, and references therein), including the MIR (Miles et al. 1994; Soifer et al. 2003; Horst et al. 2009). Based on VISIR/VLT MIR observations at $12.3\text{ }\mu\text{m}$, Horst et al. (2009) report the detection of distinct knots of star formation around the nucleus located at a distance of $\sim 1.3''$ (~ 400 pc), although with low signal-to-noise. Using NIR HST data, DS07 identified 30 clusters of star formation in the ring at $1.1\text{ }\mu\text{m}$. By fitting the individual ultraviolet-to-NIR SEDs of the clusters, the authors reported the presence of a dominant intermediate age population (8-20 Myr) and a younger and more extinguished one ($\sim 1\text{-}3$ Myr). The latter does not coincide with the optical/NIR continuum-emitting regions, but seems to be traced by the MIR/radio emission, less affected by extinction than the optical/NIR.

Figure 2 shows the high resolution 8.74 and $18.3\text{ }\mu\text{m}$ T-ReCS images of NGC 7469. At both wavelengths we detect extended emission with high signal-to-noise coincident with the star-forming ring. Indeed, our flux maps appears very similar to the high resolution $11.7\text{ }\mu\text{m}$ contours presented by Miles et al. (1994) and to the high resolution ($0.2''$) VLA 8.4 GHz radio map presented in Colina et al. (2001). We identified the brightest knots in our MIR images in Figure 2 using the same notation as in Miles et al. (1994), where the AGN is labelled A. The B and C knots in our images correspond to the brightest regions in radio, according to the 5 GHz (Wilson et al. 1991) and 8.4 GHz radio maps (Colina et al. 2001). We also identified the knots D, E, and F. In Table 5 we report the star clusters identified by DS07 which better match the positions of the A to F MIR compact regions. The distances between these knots and the AGN range from $1.4''$ to $1.8''$ (median distance of ~ 480 pc). All the knots appear more compact in the $18.3\text{ }\mu\text{m}$ image than in the $8.74\text{ }\mu\text{m}$, where the ring emission is more extended. This is expected since the $8.74\text{ }\mu\text{m}$ filter contains the $8.6\text{ }\mu\text{m}$ Polycyclic Aromatic Hydrocarbon (PAH) fea-

ture, whereas the $18.3\text{ }\mu\text{m}$ filter is mostly probing hot dust emission. As found by Spitzer, the $\sim 8\text{ }\mu\text{m}$ PAH emission of nearby galaxies appears to be more extended than at $\sim 24\text{ }\mu\text{m}$ (e.g., Helou et al. 2004; Calzetti et al. 2005).

In Table 5 we report aperture fluxes for the six identified knots in both the 8.74 and $18.3\text{ }\mu\text{m}$ images calculated using IRAF¹². The aperture radius was defined on the basis of the resolution element in the Qa band ($0.55''$), and corresponding aperture corrections were applied, since the knots are only barely resolved in both bands. Positions relative to the nucleus (A) in arcseconds are also given.

3.2. NGC 6221

The galaxy NGC 6221 is a prototypical example of the so-called “X-ray-loud composite galaxies” (see e.g., Moran et al. 1996). This classification comes from the comparison between its optical spectrum, which is starburst-like, and its X-ray data, where the AGN is revealed (Levenson et al. 2001). According to the X-ray data, and in particular the width of the Fe K α line, the orientation of the Seyfert nucleus is Type-1 (Levenson et al. 2001). However, as mentioned above, the optical spectrum of the galaxy resembles more that of a starburst galaxy, implying that there must be a big amount of dust (likely associated with the starburst) along the line of sight (LOS) hiding the BLR. A nuclear optical extinction of $A_V=3.0$ mag was measured from the optical spectrum by Levenson et al. (2001). They also presented HST images of the central region of NGC 6221 in the optical (F606W/WFPC2) and in the NIR (F160W/NICMOS) and identified the bright central NIR source as the AGN. At optical wavelengths, the nucleus is diffuse and weaker than other bright knots, identified as star clusters.

Our 8.7 and $18.3\text{ }\mu\text{m}$ images of NGC 6221 are shown in Figure 3. They reveal spectacular extended emission with two bright knots. The AGN is centered in both images. The other bright knot, at $\sim 1.9''$ SW from the nucleus, which is roughly coincident with the SW starburst region shown in the F606W optical image in Figure 3 of Levenson et al. (2001), reaches practically the same intensity as the AGN at $8.7\text{ }\mu\text{m}$ and appears brighter at $18.3\text{ }\mu\text{m}$. We measured aperture fluxes in a $0.7''$ radius for the SW knot, selected to collect the bulk of its MIR emission, and obtain fluxes of 42 mJy at $8.7\text{ }\mu\text{m}$ and 422 mJy at $18.3\text{ }\mu\text{m}$. Surrounding the AGN there is more diffuse emission extending towards the North, which in this case is more intense in the $8.7\text{ }\mu\text{m}$ image than in the $18.3\text{ }\mu\text{m}$ one. As already mentioned in Section 3.1, the $\sim 8\text{ }\mu\text{m}$ PAH emission of nearby galaxies appears more extended than the $\sim 24\text{ }\mu\text{m}$ emission (e.g., Helou et al. 2004; Calzetti et al. 2005).

4. SED OBSERVATIONAL PROPERTIES

4.1. Average Seyfert 1 Spectral Energy Distribution

Using the MIR and NIR data reported in Tables 3 and 4 we construct subarcsecond resolution nuclear SEDs in the wavelength range from ~ 1 to $18\text{ }\mu\text{m}$ for the five Type-1 Seyferts analyzed here. Figure 4 shows a comparison

¹² IRAF is distributed by the National Optical Astronomy Observatory, which is operated by the Association of Universities for the Research in Astronomy, Inc., under cooperative agreement with the National Science Foundation (<http://iraf.noao.edu/>).

TABLE 4
HIGH SPATIAL RESOLUTION NIR FLUXES

Galaxy	Flux Density (mJy)			Filters	Reference(s)	
	J band	H band	K band	L band		
NGC 1097	1.1±0.1	2.7±0.1	3.9±0.1	11±1	NACO J,H,K,L'	a
NGC 1566	1.1±0.1	...	2.1±0.1	7.8±0.1	NACO J,K,L'	a
NGC 6221	...	2.1±0.2	F160W	b
NGC 6814	...	5.2±0.5	F160W	b
NGC 7469 ^a	8.0±0.1	15±1	20±1	84±1	NACO J,H,K,L'	a
NGC 3227 ^b	...	7.8±0.8	16.4±1.7	46.7±9.3	F160W,F222M, NSFCam L	c,d
NGC 4151 ^b	60±6	100±10	197±20	325±65	F110W,F160W,F222M, NSFCam L	c,e

REFERENCES. — (a) Prieto et al. (2010); (b) This work; (c) Kishimoto et al. (2007); (d) Alonso-Herrero et al. (2003); (e) Ward et al. (1987)

NOTE. — Ground-based instruments and telescopes are NACO on the 8 m VLT and NSFCam on the 3 m NASA IRTF. Measurements in the F110W, F160W, and F222M filters are from NICMOS on HST.

^aPrieto et al. (2010) also reported a flux measurement of 19±1 mJy obtained from a NICMOS/HST observation in the filter F187N.

^bWard et al. (1987) also reported M-band flux measurements of 72±27 mJy for NGC 3227 and 449±34 mJy for NGC 4151 obtained with IRCAM3 on the 3.8 m UKIRT.

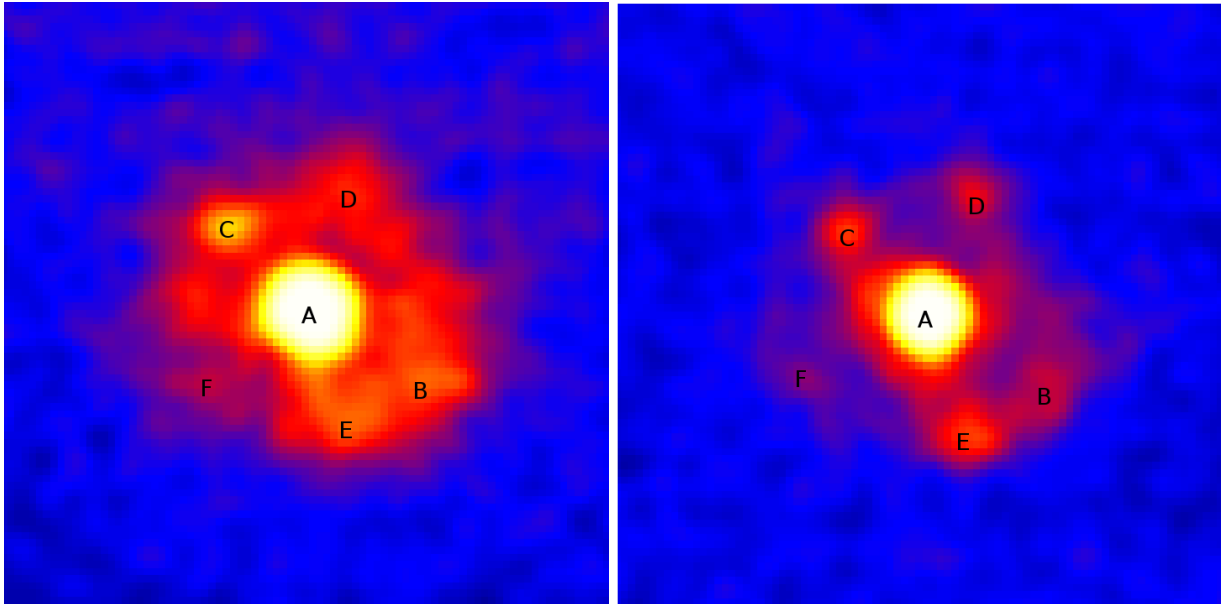


FIG. 2.— 8.74 μm (left) and 18.3 μm (right) T-ReCS images of NGC 7469 smoothed by using a moving box of 3 pixel size. The images size is 7.8 arcsec side. North is up, and East to the left. Emitting regions identified in both the Si-2 and Qa images, and also coincident with the radio emission, are labelled from A to F, where A corresponds to the AGN.

between their spectral shapes and the average Sy2 SED from RA09. This mean template was constructed using individual Sy2 data of the same angular resolution as that achieved in this work ($\lesssim 0.55''$). In the same way, we have constructed an average Type-1 Seyfert template using the IR nuclear SEDs of the seven galaxies studied here¹³. The spectral shape of Sy1 and Sy1.5 galaxies is practically identical (as can be seen from Figure 4). Based on the previous, and on the fact that both types of nuclei present broad lines in their optical spectra, in this work we consider them as Type-1 Seyferts.

The Sy2 template defines the wavelength grid, and we performed a quadratic interpolation of nearby measurements of the individual Sy1 galaxies onto its scale (1.265,

1.60, 2.18, 3.80, 4.80, 8.74, and 18.3 μm). We did not interpolate the sparse observations of NGC 6221 and NGC 6814, which only have NICMOS 1.6 μm data in addition to the MIR measurements. The interpolated fluxes were used solely for the purpose of deriving the average Sy1 template. The error bars correspond to the standard deviation of each averaged point, except for the 8.74 μm point (the wavelength chosen for the normalization). In this case, we assigned a 15% error, which is the nominal percentage considered for the N-band flux measurements (see Section 2).

We measured the 1.265–18.3 μm IR slope ($f_{\nu} \propto \nu^{-\alpha_{IR}}$) of the Sy1 template, which is representative of the individual Sy1 SEDs: $\alpha_{IR} = 1.7 \pm 0.3$. We also calculated the NIR ($\alpha_{NIR} = 1.6 \pm 0.2$, from 1.265 to 8.74 μm) and MIR spectral indexes ($\alpha_{MIR} = 2.0 \pm 0.2$, using the 8.7 and 18.3 μm points). A flat NIR slope indicates an important contribution of hot dust emission (up to ~ 1000 -1200

¹³ We have not considered the NIR ground-based data reported in Table 4 of RA09 for NGC 3227 and NGC 4151 in the construction of the mean template to be consistent with the angular resolutions of the other SEDs.

TABLE 5
POSITIONS AND FLUX DENSITIES OF NGC 7469 MIR KNOTS

Knot	ID	(X)	8.74 μm	Flux (mJy)	(X)	18.3 μm	Flux (mJy)
	DS07	(Y)			(Y)		
A	...	0.00	0.00	229	0.00	0.00	1320
B	C20	-1.58''	-0.89''	11.9	-1.54''	-0.93''	50
C	C6	1.09''	1.07''	13.4	0.95''	1.06''	79
D	C10	-0.49''	1.31''	11.5	-0.58''	1.38''	107
E	C7,C15	-0.40''	-1.36''	15.8	-0.52''	-1.49''	104
F	C12	1.25''	-0.89''	3.7	1.47''	-0.83''	14.8

NOTE. — Columns (1) and (2) indicate the label assigned to each knot in Figure 2 and in DS07. B, C, and D are also coincident with the R3, R2, and R1 regions in the VLA 8.4 GHz radio maps in Colina et al. (2001). Columns (3,4) and (6,7) indicate the position of each knot relative to A at 8.7 and 18.3 μm , respectively. Columns (5) and (8) list the flux densities of the knots in a 0.55'' aperture radius. Fluxes include aperture corrections of 19% at 8.7 μm and 37% at 18.3 μm . Errors in flux densities are dominated by uncertainties in the flux calibration (\sim 5-10% at 8.7 μm and \sim 15-20% at 18.3 μm).

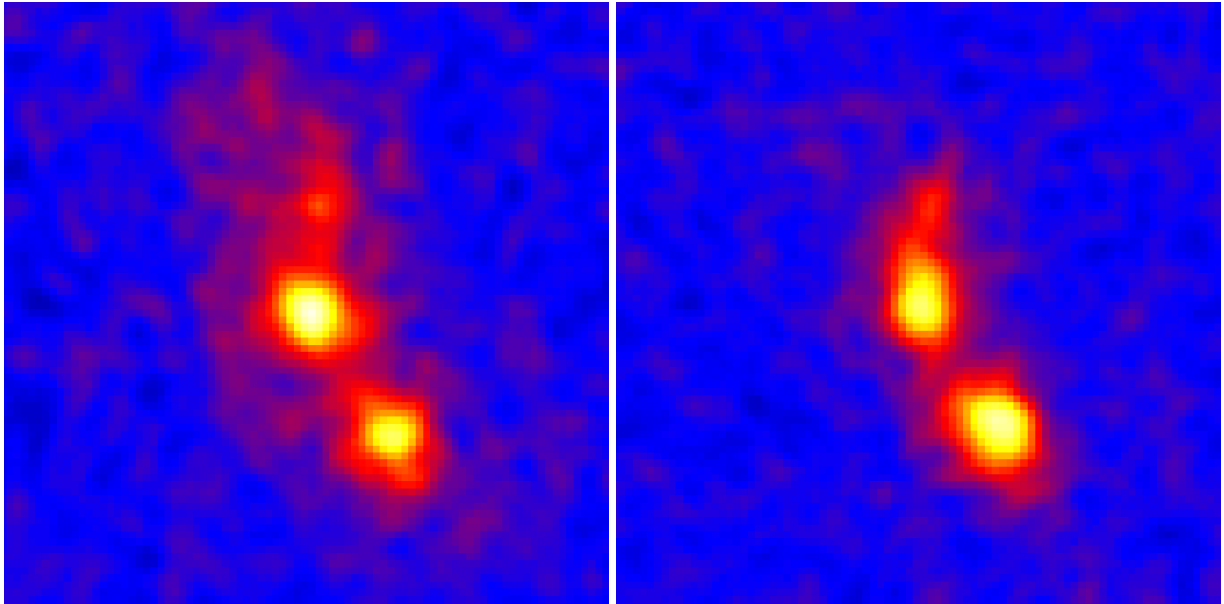


FIG. 3.— 8.74 μm (left) and 18.3 μm (right) T-ReCS images of NGC 6221 smoothed by using a moving box of 3 pixel size. The images size is 7.8 arcsec up, and East to the left. The AGN is centered in both images.

K; Rieke & Lebofsky 1981; Barvainis 1987) that comes from the immediate vicinity of the AGN. α_{IR} , α_{NIR} , and α_{MIR} values for the individual Type-1 Seyfert galaxies and for the mean Sy1 and Sy2 SEDs are shown in Table 6. The shape of the Sy2 mean SED is very steep ($\alpha_{IR} = 3.1 \pm 0.9$, $\alpha_{NIR} = 3.6 \pm 0.8$, and $\alpha_{MIR} = 2.0 \pm 0.2$) compared with those of the Type-1 Seyferts. In general, Sy2 have steeper 1–10 μm SEDs than Sy1 (Rieke 1978; Edelson et al. 1987; Ward et al. 1987; Fadda et al. 1998; Alonso-Herrero et al. 2001, 2003). On the contrary, the MIR slope results to be the same ($\alpha_{MIR} = 2.0 \pm 0.2$) for both the Sy1 and Sy2 templates.

Alonso-Herrero et al. (2003) also reported IR spectral indices measured from 1 to 16 μm for Sy1 and Sy1.5 galaxies ($\alpha_{IR}^{Alonso} = 1.5$ –1.6). On the other hand, the NIR slopes of the Sy1.8 and Sy1.9 in RA09 have intermediate values between those of Sy2 and Sy1 (mean slope $\alpha_{IR} = 2.0 \pm 0.4$), also in agreement with the IR slopes reported in Alonso-Herrero et al. (2003) for Sy1.8 and Sy1.9 ($\alpha_{IR}^{Alonso} = 1.8$ –2.6). In summary, the slope of the

IR nuclear SED is generally correlated with Seyfert type: Type-2 nuclei show steeper SEDs, whereas Type-1 and intermediate Seyferts are flatter. The NIR excess responsible for flattening the SED of the Type-1 nuclei would come from the contribution of hot dust in the directly-illuminated faces of the clouds in the torus, as well as from the direct AGN emission (i.e., the tail of the optical power-law continuum).

A similar comparison between Type-1 and Type-2 spectral shapes can be done by using the H/N and N/Q flux ratios. H/N is larger for Type-1 Seyferts (0.07 ± 0.03) than for Sy2 (0.003 ± 0.002), as measured from the individual values of the Sy1 considered here and the Sy2 in RA09. The difference in H/N between Sy1 and Sy2 galaxies is significantly different at the 100% confidence level, according to the Kolmogorov-Smirnov (K-S) test. This ratio depends on both the torus inclination and covering factor, as we will discuss in Section 6.1. On the other hand, N/Q is very similar for Type-1 and Type-2 Seyferts (mean values of 0.27 ± 0.11 and 0.23 ± 0.14 respec-

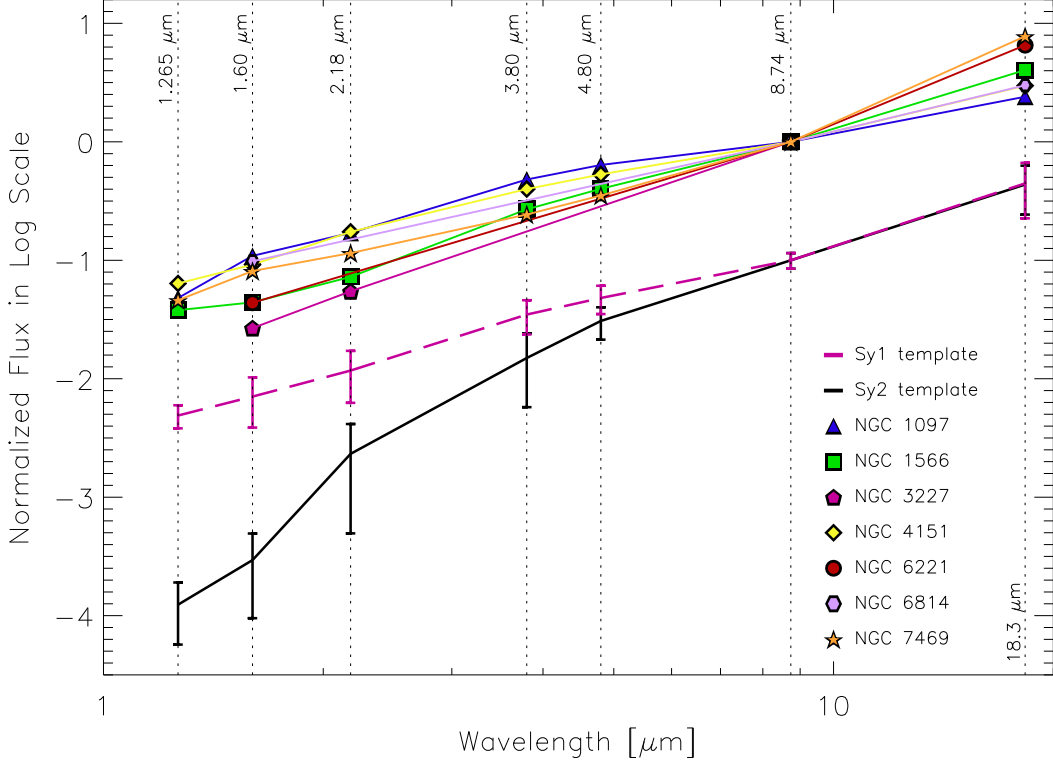


FIG. 4.— Observed IR SEDs for the seven Type-1 Seyfert galaxies (in color and with different symbols) used for the construction of the Sy1 average template (dashed pink). The Sy2 template from RA09 (solid black) is also plotted for comparison. The SEDs have been normalized at $8.74 \mu\text{m}$, and the average Sy1 and Sy2 SEDs have been shifted in the Y-axis for clarity.

TABLE 6
SPECTRAL SHAPE INFORMATION

Galaxy	α_{IR}	α_{NIR}	α_{MIR}	H/N	N/Q
Average Sy2	3.1 ± 0.9	3.6 ± 0.8	2.0 ± 0.2	0.003	0.23
Average Sy1	1.7 ± 0.3	1.6 ± 0.2	2.0 ± 0.2	0.071	0.22
NGC 1097	1.4 ± 0.2	1.6 ± 0.2	1.2 ± 0.1	0.117	0.42
NGC 1566	1.8 ± 0.3	1.8 ± 0.3	1.9 ± 0.2	0.040 ^a	0.25
NGC 3227	2.0 ± 0.4	2.0 ± 0.4	...	0.019	...
NGC 4151	1.4 ± 0.2	1.4 ± 0.1	1.5 ± 0.1	0.076	0.41
NGC 6221	2.0 ± 0.5	1.8 ± 0.4	2.5 ± 0.3	0.044	0.15
NGC 6814	1.4 ± 0.2	1.4 ± 0.2	1.5 ± 0.1	0.098	0.33
NGC 7469	1.8 ± 0.3	1.5 ± 0.2	2.8 ± 0.4	0.086	0.13

NOTE. — Columns 2, 3, and 4 show the fitted spectral indexes ($f_\nu \propto \nu^{-\alpha}$) measured from the average Sy2 and Sy1 templates and for the individual Sy1 SEDs in the whole range (α_{IR} , from ~ 1 to $18 \mu\text{m}$), in the NIR (α_{NIR} , from ~ 1 to $\sim 9 \mu\text{m}$), and in the MIR (α_{MIR} , using the N and Q band data points) respectively. Columns 5 and 6 give the values of the H/N and N/Q band ratios.

^aDue to the lack of H-band data for NGC 1566, we used the interpolated value at $1.6 \mu\text{m}$ for calculating the H/N.

tively). Values of H/N and N/Q for the individual Sy1 galaxies and the average templates are reported in Table 6.

5. SED MODELLING

5.1. Clumpy Dusty Torus Models and Bayesian approach

The clumpy dusty torus models of Nenkova et al. (2002) hold that the dust surrounding the central engine of an AGN is distributed in clumps, instead of homogeneously filling the torus volume. These clumps are dis-

tributed with a radial extent $Y = R_o/R_d$, where R_o and R_d are the outer and inner radius of the toroidal distribution, respectively (see Figure 5). The inner radius is defined by the dust sublimation temperature ($T_{sub} \approx 1500 \text{ K}$), with $R_d = 0.4 (1500 \text{ K} T_{sub}^{-1})^{2.6} (L/10^{45} \text{ erg s}^{-1})^{0.5} \text{ pc}$. Within this geometry, each clump has the same optical depth (τ_V , defined at the V-band). The average number of clouds along a radial equatorial ray is N_0 . The radial density profile is a power-law ($\propto r^{-q}$). A width parameter, σ , characterizes the angular distribution of the clouds, which has a smooth edge. The number of clouds along the LOS at an inclination angle i is $N_{LOS}(i) = N_0 e^{-(i-90)^2/\sigma^2}$. Finally, the optical extinction produced by the torus along the LOS is computed as $A_V^{LOS} = 1.086 N_0 \tau_V e^{-(i-90)^2/\sigma^2} \text{ mag}$. For a detailed description of the clumpy models see Nenkova et al. (2002, 2008a,b).

The clumpy database now contains 1.2×10^6 models, calculated for a fine grid of model parameters. The inherent degeneracy between these parameters has to be taken into account when fitting the observables. To this end, we recently developed a Bayesian inference tool (BayesClumpy), that extracts as much information as possible from the observations. Details on the interpolation methods and algorithms employed can be found in Asensio Ramos & Ramos Almeida (2009). Thus, for the following analysis of the Seyfert SEDs, we are not using the original set of models described in Nenkova et al. (2008a,b), but an interpolated version of them (See Figures 3 and 4 in Asensio Ramos & Ramos Almeida 2009 for a comparison between the original and interpolated

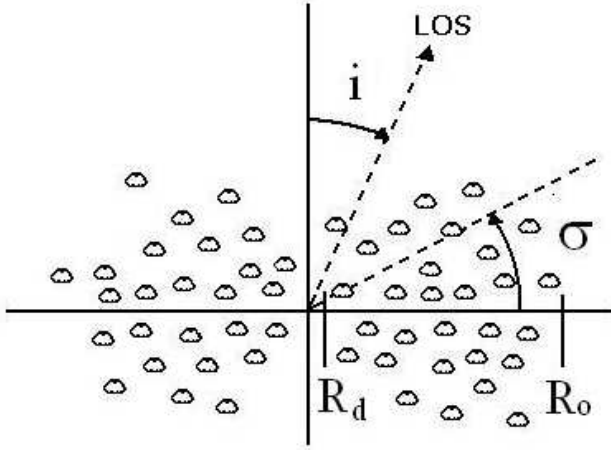


FIG. 5.— Scheme of the clumpy torus described in Nenkova et al. (2008a,b). The radial extent of the torus is defined by the outer radius (R_o) and the dust sublimation radius (R_d). All the clouds are supposed to have the same τ_V , and σ characterizes the width of the angular distribution. The number of cloud encounters is function of the viewing angle, i .

models). In this work we use the most up-to-date version of the models that are corrected for a mistake in the torus emission calculations, which in principle only affects the AGN scaling factor (see erratum by Nenkova et al. 2010). The present version of BayesClumpy has also been updated to use the Multinest algorithm of Feroz et al. (2009) for sampling. This algorithm is very robust and efficient when sampling from complex posterior distributions.

The prior distributions for the model parameters are assumed to be truncated uniform distributions in the intervals reported in Table 7. Therefore, we give the same weight to all the values in each interval. Apart from the six parameters that characterize the models, there is an additional parameter that accounts for the vertical displacement required to match the fluxes of a chosen model to an observed SED, which we allow to vary freely. This vertical shift scales with the AGN bolometric luminosity (see Section 6). In order to compare with the observations, BayesClumpy simulates the effect of the employed filters on the simulated SED by integrating the product of the synthetic SED and the filter transmission curve. Observational errors are assumed to be Gaussian or upper/lower limit detections. A detailed description of the Bayesian inference applied to the clumpy models can be found in Asensio Ramos & Ramos Almeida (2009). Additionally, to see an example of the use of clumpy model fitting to IR SEDs using BayesClumpy, see RA09.

5.2. Model Results

5.2.1. Seyfert 1 Individual Fits

The results of the fitting process of the IR SEDs with the interpolated version of the clumpy models of Nenkova et al. (2008a,b) are the posterior distributions for the six free parameters that describe the models and the vertical shift. These are indeed the probability distributions of each parameter, represented as histograms. When the observed data introduce sufficient information into the fit, the resulting posteriors will clearly differ from the input uniform priors, either showing trends or being cen-

tered at certain values within the intervals considered. For all the Sy1 fits, we considered uniform priors in the intervals shown in Table 7. The only exception is NGC 7469, for which we use a gaussian prior of $85^\circ \pm 2^\circ$ for the inclination angle of the torus, based on the value of the accretion disk viewing angle deduced from X-ray observations (Nandra et al. 2007), assuming that the disk and the torus are coplanar.

We fit the individual Sy1 SEDs with BayesClumpy, modelling the torus emission and the direct AGN contribution (the latter as a broken power law). We also consider the IR extinction curve of Chiar & Tielens (2006) to take into account any possible foreground extinction from the host galaxy. The AGN scales self-consistently with the torus flux, and the foreground extinction (separate from the clumpy torus) is another free parameter, which we set as a uniform prior ranging from $A_V=0$ to 10 mag¹⁴.

In addition to the Gemini MIR unresolved fluxes reported in Table 3 we consider MIR nuclear fluxes from VISIR compiled from the literature when available (see Table A1 in Appendix A) We find good agreement between the VISIR and T-ReCS unresolved fluxes. We did not include measurements in the VISIR PAH filters (8.59, 11.25 and 11.88 μm) for the galaxies NGC 7469 and NGC 1097 because of their intense star formation and their already well-sampled SED.

Although the solutions to the Bayesian inference problem are the probability distributions of each parameter, we can translate the results into corresponding spectra (Figures 6 and 7). The solid lines correspond to the model described by the combination of parameters that maximizes their probability distributions (maximum-a-posteriori; MAP). Dashed lines represent the model computed with the median value of the probability distribution of each parameter. Shaded regions indicate the range of models compatible with the 68% confidence interval for each parameter around the median. In Figure 8 we show the posteriors of the six torus parameters (the vertical shift and the foreground extinction have been marginalized) for the galaxy NGC 1097. Those for the rest of the Sy1 galaxies are presented in Appendix A (Figures A1 to A6).

The more information the IR SEDs provide, the better the probability distributions are constrained. From the analysis performed here and in RA09 it appears important to sample the SED in the wavelength range around 3-4 μm and also at $\sim 18 \mu\text{m}$ to constrain the model parameters. A detailed study of the influence of different filters/wavelengths in the restriction of the clumpy models parameter space will be the subject of a forthcoming paper (Asensio Ramos et al., in prep.). The posterior information for the seven Sy1 galaxies is summarized in Table 8.

From the individual fits of the Sy1 galaxies in our sample with clumpy torus models we obtain the following results:

1. The average number of clouds along an equatorial ray is within the interval $N_0=[1, 8]$,

¹⁴ Note that A_V is the foreground extinction from the host galaxy, which is different from the A_V^{LOS} value reported in Table 8, corresponding to the extinction produced by the torus. $A_V^{LOS} = 1.086 N_0 \tau_V e^{(-(i-90)^2/\sigma^2)} \text{ mag}$.

TABLE 7
CLUMPY MODEL PARAMETERS AND CONSIDERED INTERVALS

Parameter	Abbreviation	Interval
Width of the angular distribution of clouds	σ	[15°, 70°]
Radial extent of the torus	Y	[5, 30]
Number of clouds along the radial equatorial direction	N_0	[1, 15]
Power-law index of the radial density profile	q	[0, 3]
Inclination angle of the torus	i	[0°, 90°]
Optical depth per single cloud	τ_V	[5, 150]

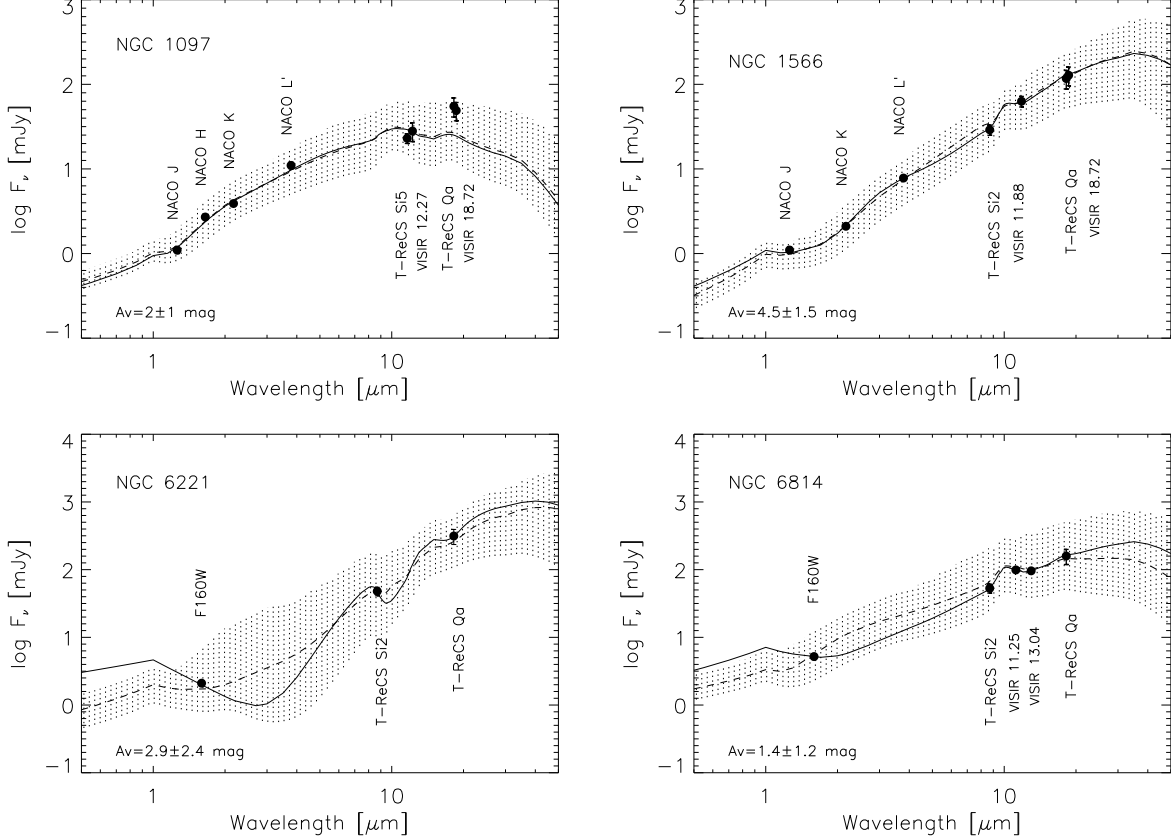


FIG. 6.— High spatial resolution IR SEDs of the Sy1 galaxies NGC 1097, NGC 1566, NGC 6221, and NGC 6814. Solid and dashed lines correspond to the MAP and median models, respectively. Shaded regions indicate the range of models compatible with the 68% confidence interval for each parameter.

2. Low values of σ are preferred: $\sigma \simeq [25^\circ, 45^\circ]$, and intermediate inclination angles of the torus are found: $i \simeq [35^\circ, 85^\circ]$.
3. The radial extent of the torus ($Y=R_o/R_d$) is weakly constrained within the interval $Y \simeq [15, 20]$.
4. Values in the range from $\tau_V \simeq [40, 140]$ are found for the optical depth of each cloud for all the galaxies.
5. The radial density profile appears constrained within the interval $q=[0.2, 1.9]$, with the only exception of NGC 1097, for which $q=2.7 \pm 0.2$.
6. The $10\ \mu\text{m}$ silicate feature appears in shallow emission or absent in the fitted models with the exception of NGC 6221 MAP model. The weak silicate feature arises in the clumpy models because both

illuminated and dark cloud sides contribute to the observed spectrum (see Section 5.4 in RA09 for a detailed discussion on the silicate feature modelling).

7. The optical extinction produced by the torus along the LOS results in $A_V^{LOS} < 690$ mag for all the galaxies.
8. The foreground extinction from the host galaxy, which obscures the AGN direct emission in our modelling, results in $A_V < 5$ mag (see Figures 6 and 7). The values derived are consistent with those published in the literature, e.g. the nuclear optical extinction of $A_V=3$ mag measured from the optical spectrum of NGC 6221 (Levenson et al. 2001), $A_V \sim 1$ mag determined from NACO/VLT colour maps (Prieto et al. 2005) for NGC 1097, and $A_V=4.5-4.9$ mag reported by Mundell et al. (1995)

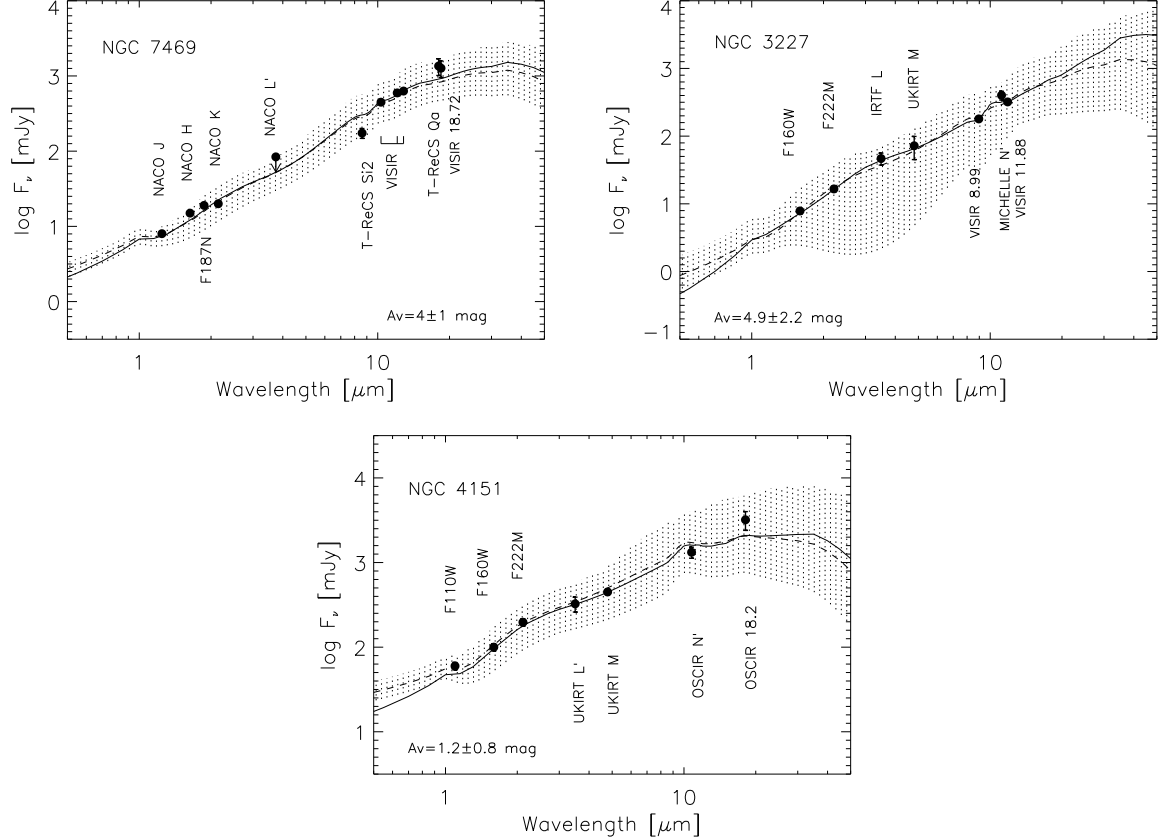


FIG. 7.— Same as in Figure 6, but for NGC 7469, NGC 3227, and NGC 4151.

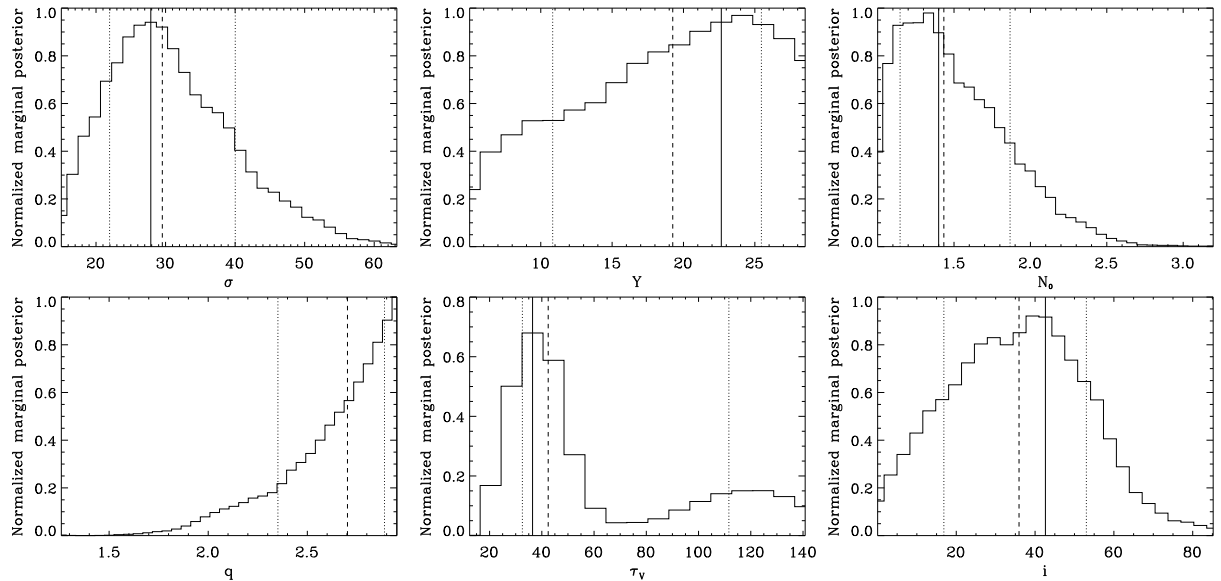


FIG. 8.— Probability distributions resulting from the fit of NGC 1097. Solid and dashed lines represent the mode and the median of each distribution and dotted lines indicate the 68% confidence level around the median. The histograms have been smoothed for presentation purposes, occasionally leading to small offsets between the solid line corresponding to the mode and the position of the maximum of the histograms.

for NGC 3227.

All the above intervals or limits of the parameters correspond to median values. We chose the medians instead of the MAPs because the former gives a less biased information about the result, since it takes into account degeneracies, while the MAP

does not.

The clumpy models successfully reproduce the observed Sy1 SEDs studied here with compatible results among them. This is indicating that the NIR and MIR unresolved fluxes employed here are dominated by a combination of reprocessed emission from dust in the torus and

TABLE 8
PARAMETERS DERIVED FROM THE CLUMPY MODEL FITTING

Galaxy	σ (°) Median	σ (°) Mode	Y Median	Y Mode	N_0 Median	N_0 Mode	q Median	q Mode	i (°) Median	i (°) Mode	τ_V Median	τ_V Mode	A_V^{LOS} (mag) Median	A_V^{LOS} (mag) Mode
NGC 1097	29 ± 10	28	19 ± 6	23	< 2	1	2.7 ± 0.2	2.9	36 ± 17	43	42 ± 69	36	<15	1
NGC 1566	46 ± 12	52	21 ± 4	20	2 ± 1	2	0.2 ± 0.2	0.1	79 ± 19	86	104 ± 28	141	165 ± 95	160
NGC 6221	42 ± 15	36	21 ± 5	24	8 ± 3	7	0.8 ± 0.7	0.4	59 ± 18	79	110 ± 33	128	<690	1
NGC 6814	23 ± 13	20	18 ± 7	23	2 ± 1	2	1.1 ± 0.6	1.1	43 ± 25	39	113 ± 32	139	<85	1
NGC 7469	41 ± 17	38	22 ± 5	27	3 ± 1	3	1.9 ± 0.4	1.9	84 ± 2 (fix)	84	141 ± 6	148	500 ± 120	430
NGC 3227	36 ± 18	33	19 ± 6	19	5 ± 4	2	0.6 ± 0.5	0.5	49 ± 21	66	118 ± 18	129	<240	1
NGC 4151	24 ± 6	19	16 ± 8	8	2 ± 1	2	1.8 ± 0.6	1.8	43 ± 18	57	110 ± 23	123	<60	1

NOTE. — Medians and modes of the Sy1 probability distributions. Those presenting single tails have been characterized with the mode and upper/lower limit at 68% confidence. The models include the intrinsic AGN continuum emission.

direct AGN emission.

Our modelling results for NGC 1097 somehow contradict those presented in Mason et al. (2007). The latter authors unsuccessfully tried to reproduce the T-ReCS 11.66 and 18.3 μm aperture fluxes that they measured for this galaxy using the clumpy models of Nenkova et al. (2002). The difference with our result is probably due to i) the fact that we obtained unresolved fluxes using PSF subtraction over the same images presented in Mason et al. (2007), reducing the potential contamination from star formation; ii) they did not consider NIR data, but only the MIR fluxes; and finally iii) they faced the degeneracy problem of the clumpy models without using any sophisticated tool as e.g. BayesClumpy.

5.2.2. Sy2 and intermediate-type Seyfert results

As a consequence of the publication of the erratum Nenkova et al. (2010), where the authors report a mistake in the torus emission calculations, we repeated all the fits presented in RA09 using our updated version of BayesClumpy. In order to do a proper comparison with the results for the Sy1 galaxies presented here, we performed the fits of the Sy2 and intermediate-type Seyferts considering exactly the same priors as for the Sy1. As in RA09, we did not consider the direct AGN contribution for either Sy1.8/1.9 or Sy2.

For the new fits we considered MIR nuclear fluxes from VISIR when available, in addition to the NIR and MIR fluxes reported in RA09. We did not include measurements in the VISIR PAH filters (8.59, 11.25 and 11.88 μm) for those galaxies with very intense star formation such as NGC 7582. Many of the SEDs in RA09 have been also updated with NIR data from recent publications. In Table B1 (Appendix B) we report the NIR-to-MIR SEDs for all the sample.

In general, the results from the fitting with the most up-to-date version of the interpolated clumpy models, which are reported in Table B2 in Appendix B, are compatible with those presented in RA09 at the 1-sigma level. Indeed, if we compare the results for the five galaxies for which we fitted exactly the same SEDs as in the previous work (Circinus, Mrk 573, NGC 1386, NGC 1808, and NGC 1365) we find that they are practically identical. The only fits that are completely different from those presented in the previous work correspond to Centaurus A and NGC 3281. This is a consequence of adding new MIR data from VISIR and/or apriori information for the inclination angle of the torus (see Appendix B).

In Table 9 we show the ranges of the parameters found for the Sy1, intermediate-type Seyferts, and Sy2. We have excluded the unreliable fits of NGC 1808 and NGC 7582 as we did in RA09. In the case of NGC 1808, due to the intense star formation that is taking place in its nuclear region and to the lower spatial resolution IR SED (all from 3-4 m telescopes), it is likely contaminated with starlight, resulting in its peculiar shape. For NGC 7582, the intense circumnuclear star formation and the edge-on orientation of the galaxy make it difficult to isolate the torus emission from that of the host galaxy. In the fit, the silicate feature is predicted in emission, while from MIR spectroscopy shows it in strong absorption (Siebenmorgen et al. 2004).

We considered the Sy1.8 and Sy1.9 types as a separate group in between the Sy1 & Sy1.5 and Sy2 because the IR slopes measured from their SEDs are intermediate between those of Sy1 and Sy2, as measured for our sample and also as reported in the literature (Section 4.1 and references therein). By looking at the ranges of parameters for the Sy1.8 and Sy1.9 types, we find similarities with the Sy1 & Sy1.5 group in Y , N_0 , and τ_V , whereas σ and q are more similar to those of Sy2.

6. COMPARISON BETWEEN TYPE-1 AND TYPE-2 SEYFERT NUCLEI

The main aim of this work is to enlarge the number of Type-1 Seyferts in the original sample of RA09 in order to better compare between Type-1 and Type-2 tori under the assumption that the SEDs studied here are torus/AGN dominated. Despite the relatively low number of objects considered (7 Type-1 and 9 Type-2 Seyferts¹⁵), we find that some of the parameters are significantly different between Sy1 and Sy2.

To take full advantage of the Bayesian approach employed here for the individual fits, the best way to compare the results for Sy1 and Sy2 galaxies is to derive joint posterior distributions for the full Type-1 and Type-2 datasets respectively. If D_i contains the observed data from the i -th SED, assuming that the different SEDs are statistically independent, we can use the Bayes theorem to write the posterior for all galaxies together as:

$$p(\boldsymbol{\theta} | \{D_i\}) \propto p(\{D_i\} | \boldsymbol{\theta}) p(\boldsymbol{\theta}) = \prod_{i=1}^N p(D_i | \boldsymbol{\theta}) p(\boldsymbol{\theta}), \quad (1)$$

where $\boldsymbol{\theta} = (\sigma, Y, N_0, q, \tau_V, i)$.

¹⁵ Here we consider the nine Sy2 in RA09 with reliable fits (NGC 1808 and NGC 7582 are excluded).

TABLE 9
RANGES OF PARAMETERS FOR SY1, INTERMEDIATE-TYPE SEYFERTS, AND SY2

Type	Galaxies	σ ($^{\circ}$)	Y	N_0	q	i ($^{\circ}$)	τ_V
Sy1 & Sy1.5	7	[25, 45]	[15, 20]	[1, 8]	[0.2, 1.9] ^a	[35, 85]	[40, 140]
Sy1.8 & Sy1.9	3	[35, 70]	[20, 25]	[1, 7]	[0.9, 3.0]	[25, 85]	[40, 85]
Sy2	9	[20, 65]	[10, 20]	[6, 14]	[0.0, 3.0]	[45, 85]	[5, 95]

NOTE. — General ranges of parameters resulting from the fits with the clumpy models for the seven Type-1 Seyferts, the three Sy1.8 and Sy1.9 nuclei, and for the nine Sy2 with reliable fits (the extremes of the intervals have been rounded to simplify the comparison). All the above intervals correspond to median values.

^aWith the exception of NGC 1097, for which $q=2.7\pm0.2$.

Thus, we normalized all the Sy1 SEDs at 8.74 μ m and fitted them together using BayesClumpy, and we did the same for the Sy2. For those galaxies without flux measurements in the Si-2 filter we performed a quadratic interpolation of the SED and used the interpolated values at 8.74 μ m to normalize the real data. We did not use the interpolated values in the fits. We considered the mean redshift for the Sy1 ($z=0.0061\pm0.0045$) and for the Sy2 (0.0078 ± 0.0051) in the fits¹⁶. In Figure 9 we show the Sy1 (left panel) and Sy2 fits (right panel). Note that the MAP and median models predict a flat SED with the silicate feature in weak emission for the Sy1 galaxies, and steeper and with the silicate band in shallow absorption for Sy2.

The comparison between the Sy1 and Sy2 posterior distributions is shown in Figure 10. From a visual inspection it is clear that the joint posteriors of the parameters N_0 , q , τ_V , and σ are completely different between Sy1 and Sy2. There is not overlap between the 1-sigma intervals. In Table 10 we report the median and mode values of the histograms in Figure 10.

In order to quantify how different the probability distributions are, we calculated the Kullback-Leibler divergence (KLD; Kullback & Leibler 1951) between the Sy1 and Sy2 posteriors. This divergence takes into account the full shape of the posterior and it is always a positive value, and it is equal to zero when two distributions are identical. Therefore, the larger the value of KLD, the more different the posteriors. We find $KLD>1$ for σ ($KLD=5.2$), N_0 ($KLD=25$), q ($KLD=1.2$), and τ_V ($KLD=21$). These are indeed the four parameters whose 1-sigma regions do not overlap (see Figure 10) and thus we consider their differences significant between Sy1 and Sy2¹⁷. For both Y and i we find $KLD<1$ and similar median values between Sy1 and Sy2.

Sy1 tori are narrower and have fewer clouds ($\sigma=44^{\circ}\pm8^{\circ}$; $N_0=4\pm1$) than those of Sy2 ($\sigma=63^{\circ}\pm4^{\circ}$; $N_0=11\pm1$). The radial density distribution of the clouds is also different between the two Seyfert types according to this analysis: in Sy2, the majority of the clumps are distributed very close to the nucleus (i.e. steep radial density distribution; $q=2.3\pm0.1$) whereas for Sy1 the clouds distribution is flatter ($q=0.8\pm0.2$). On the other hand, the optical depth of the clouds in Sy1 tori is larger ($\tau_V=133\pm8$) than in Sy2 ($\tau_V=30\pm1$).

By taking a closer look to the right panel of Figure 9,

¹⁶ Indeed, since all the galaxies are local Seyferts, the results are the same if we consider that the SEDs are rest-frame

¹⁷ See further discussion on the Sy2 q parameter results below.

which corresponds to the Sy2 fit, it is clear that some of the data points are underestimated by the model. This happens because of the Circinus SED, which has the shortest errors bars, has more weight in the fit than the rest of the SEDs. In order to check that our Sy2 results are not completely biased by Circinus, we have repeated the fit excluding it, as well as NGC 1386, which is the least restricted SED in terms of data points, getting rid of the extremes. From the new fit, we find even larger differences with the Sy1 values of σ , N_0 , and τ_V . On the other hand, the q joint posterior becomes comparable to that of the Sy1, probably as a consequence of getting rid of the two SEDs fitted with the largest q values among the Sy2. Considering all the previous we prefer to be cautious about the q parameter, and only consider σ , N_0 , and τ_V genuinely different between Sy1 and Sy2.

Interestingly, we find high as well as low values of the inclination angle of the torus for Sy1 and Sy2 (see Table 9). This variety in the i values translates into the similar median values found for the joint Sy1 and Sy2 posterior distributions ($47^{\circ}\pm6^{\circ}$ for Sy1 and $54^{\circ}\pm10^{\circ}$ for Sy2), which are also intermediate within the considered prior ($i=[0^{\circ}, 90^{\circ}]$). *This is telling us that, in the clumpy torus scenario, the classification of a Seyfert galaxy as a Type-1 or Type-2 depends more on the intrinsic properties of the torus rather than in its inclination.*

Our results contradict those presented by Hönig et al. (2010), who find similar averaged values of N_0 for both the Sy1 and Sy2 galaxies in their sample. However, it is worth mentioning that they fixed low values of the inclination angle of the torus for Sy1 and large for Sy2, what can likely have influenced their results.

In Figure 11 we represent the median values of σ and N_0 for the different Seyfert types over the covering factor contours¹⁸. The covering factor is defined as $C_T = 1 - \int e^{-N_{LOS}(i)} d\cos(i)$. Type-1 nuclei tend to be located within lower C_T contours ($C_T \leq 0.6$) than those of Type-2s, for which $C_T \geq 0.5$, with the exception of Centaurus A and Mrk 573¹⁹. We have represented with

¹⁸ A similar plot showing values for Sy2 galaxies from RA09 and PG quasars from Mor et al. (2009) was shown in the talk by M. Elitzur at the Physics of Galactic Nuclei conference held 15–19 June, 2009 at Ringberg Castle. Proceedings published online at http://www.mpe.mpg.de/events/pgn09/online_proceedings.html.

¹⁹ As discussed in RA09, the fit of Centaurus A is complicated by the presence of a dust lane of $A_V \sim 7-8$ mag that is likely affecting the NIR nuclear fluxes, as well as the possible synchrotron contamination of the MIR fluxes. Mrk 573 has been recently reclassified as an obscured Narrow-line Seyfert 1 (NLSy1) based on NIR spectroscopy (Ramos Almeida et al. 2008, 2009b). However,

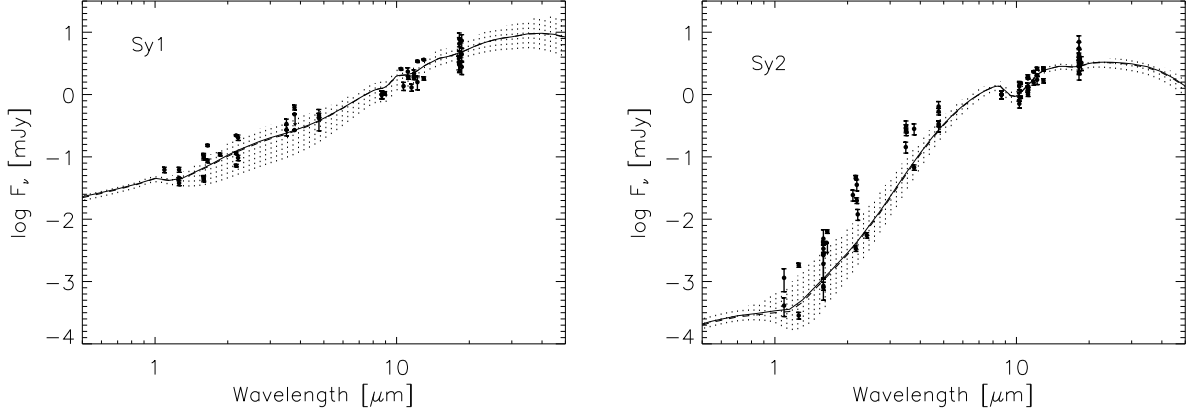


FIG. 9.— Same as in Figure 6, but for the Sy1 (left) and Sy2 SEDs (right) normalized at 8.74 μm .

TABLE 10
STATISTICS OF THE COMPARISON BETWEEN SY1 AND SY2 PARAMETERS

Type	σ ($^{\circ}$) Sy1	σ ($^{\circ}$) Sy2	Y Sy1	Y Sy2	N_0 Sy1	N_0 Sy2	q Sy1	q Sy2	i ($^{\circ}$) Sy1	i ($^{\circ}$) Sy2	τ_V Sy1	τ_V Sy2
Medians	44 ± 8	63 ± 4	21 ± 4	23 ± 4	4 ± 1	11 ± 2	0.8 ± 0.2	2.3 ± 0.1	47 ± 7	54 ± 10	133 ± 8	30 ± 1
Modes	42	65	21	29	4	11	0.9	2.2	46	55	132	30

larger symbols the median values from the joint σ and N_0 posteriors reported in Table 10.

Since the covering factor is a non-linear function of the torus parameters, we took full advantage of our Bayesian approach and generated joint posterior distributions for C_T from those in Figure 10, which are shown in the left panel of Figure 12. The median values of the histograms are $C_T(\text{Sy2})=0.95 \pm 0.02$ and $C_T(\text{Sy1})=0.5 \pm 0.1$. The divergence between the Sy1 and Sy2 C_T posteriors is $KLD=28$, indicating that the difference is significant (the 1-sigma regions do not overlap). Thus, Sy1 tori in our sample have lower C_T s than those of Sy2, implying that they are intrinsically different.

6.1. Near-infrared Emission and Torus Angular Width

As reported in Section 4.1, Type-1 Seyferts present characteristically higher H/N ratios and flatter SEDs than those of Sy2 nuclei. The enhancement on the NIR emission of Type-1 AGN is produced by the hot dust from the directly-illuminated faces of the clumps in the torus which are close to the central engine, and also by direct AGN emission (i.e., the tail of the optical/ultraviolet power-law continuum), which strongly flattens their IR SEDs (Rieke & Lebofsky 1981; Barvainis 1987).

Based on the IR SEDs presented here, the relative NIR contribution to the SED is generally correlated with the Seyfert type. Sy2 galaxies show lower NIR to MIR ratios ($H/N=0.003 \pm 0.002$) than Sy1 (0.06 ± 0.03).

In the context of the clumpy models, the presence of a cloud along the LOS, which may occur from any viewing angle, results in a Type-2 classification. *Cloud encounters are more probable at large inclination angles (i), but there is always a finite probability for having an unobscured view of the AGN.* In fact, the likelihood of inter-

here we considered it as a Sy2 because of the similarity in SED shape with the rest of the sample.

cepting a cloud along a LOS depends on the combination of i , N_0 , and σ . Thus, the preference for lower values of these parameters (especially N_0 and σ) in Type-1 Seyferts increases the likelihood of unimpeded views of some directly-illuminated cloud faces (i.e., those on the “back” side of the torus) and direct AGN emission, resulting in an increase of the NIR flux. The latter can be represented in terms of the escape probability P_{esc} (see equation 4 in Nenkova et al. 2008a). For a total number of clouds N_{LOS} along a path, $P_{esc} \simeq \exp(-N_{LOS})$ when the clouds are optically thick ($\tau_\lambda > 1$).

In Figure 13 we show the dependence of the H/N ratio on the escape probability. All the Sy2 are in the bottom-left corner of the diagram, whereas the Sy1 have higher values of the H/N ratio and $P_{esc}=[1\%, 92\%]$. Sy1.8 and Sy1.9 galaxies present intermediate values between those of Sy1 and Sy2. The derived joint posterior distributions of the escape probabilities for Sy1 and Sy2 ($KLD=29$ between them) are shown in Figure 12, and the median values of the histograms are $P_{esc}(\text{Sy1}) = 18 \pm 3\%$ and $P_{esc}(\text{Sy2}) = 0.05 \pm 0.08\%$.

Thus, while for tori with high values of i , N_0 , and σ the probability of having a direct view of the AGN is very little, that increases for objects with narrower and less inclined tori, and containing less clumps. *In this work we show for the first time that, in the clumpy torus scenario, the classification as a Type-1 or Type-2 Seyfert depends more on the intrinsic properties of the torus, rather than in the inclination angle itself.* The Sy1 galaxies in our sample have larger P_{esc} than the Type-2 Seyferts, and as a consequence of that, we detect the broad lines in their spectra.

6.2. AGN Luminosities

The clumpy model fits yield the intrinsic bolometric luminosity of AGN (L_{bol}^{AGN}) by means of the vertical shift

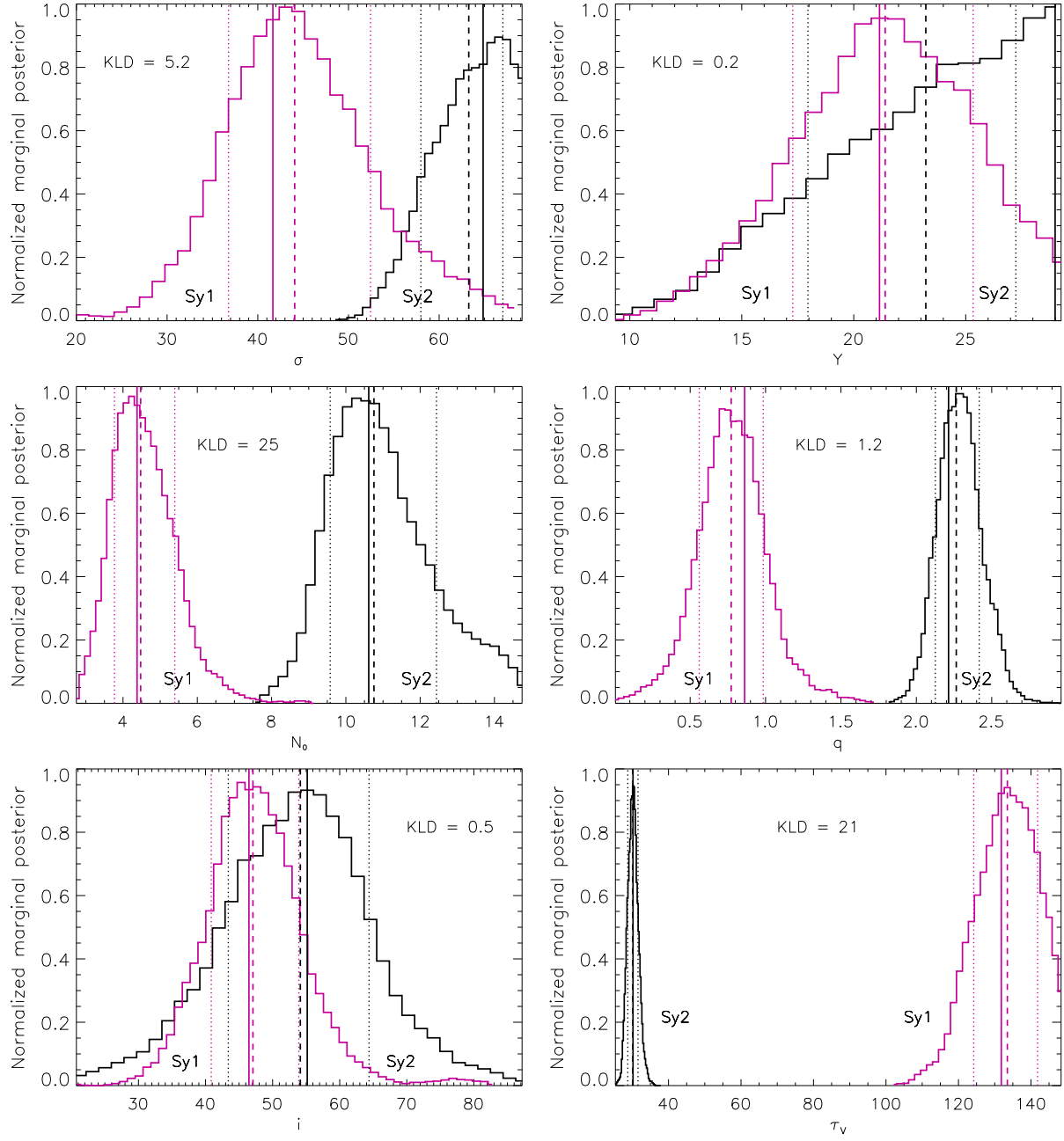


FIG. 10.— Same as in Figure 8, but for the joint Sy1 and Sy2 SEDs. KLD values derived from the comparison between Sy1 and Sy2 for each parameter are labelled.

applied to match the observational data points. Combining this value with the torus luminosity (L_{bol}^{tor}), obtained by integrating the corresponding model torus emission (without the AGN contribution), we derive the reprocessing efficiency (RE) of the torus ($L_{bol}^{tor}/L_{bol}^{AGN}$). The previous values are calculated on the Bayesian framework, by combining the posterior distributions of the model parameters. Median values and 1-sigma intervals for Sy1 galaxies are reported in Table 11, and those for Sy2 and intermediate-type Seyferts are shown in Table B3 (Appendix B).

Sy2 tori in our sample are more efficient reprocessors than Sy1, absorbing and re-emitting the majority of the intrinsic AGN luminosity in the IR: $RE(Sy2)=[0.4, 1.0]$, with a median value of 0.8 and $RE(Sy1)=[0.2, 0.7]$, with

median of 0.5. It makes no sense to compare the derived joint Sy1 and Sy2 posterior distributions of RE, because we normalized the SEDs to perform the fits, and consequently the derived L_{bol}^{AGN} are meaningless.

We considered a possible dependency of the RE (or alternatively the covering factor; C_T) on L_{bol}^{AGN} , since the amount of incoming radiation from the AGN could possibly have some influence on the reprocessed energy or even in the torus properties (e.g., receding torus scenario; Lawrence et al. 1991). However, we find no relationship between the two quantities in the luminosity range considered. This means that the reprocessing efficiency depends primarily on the total number of clouds available to absorb the incident radiation, i.e. on the torus covering factor. However, the possible dependence

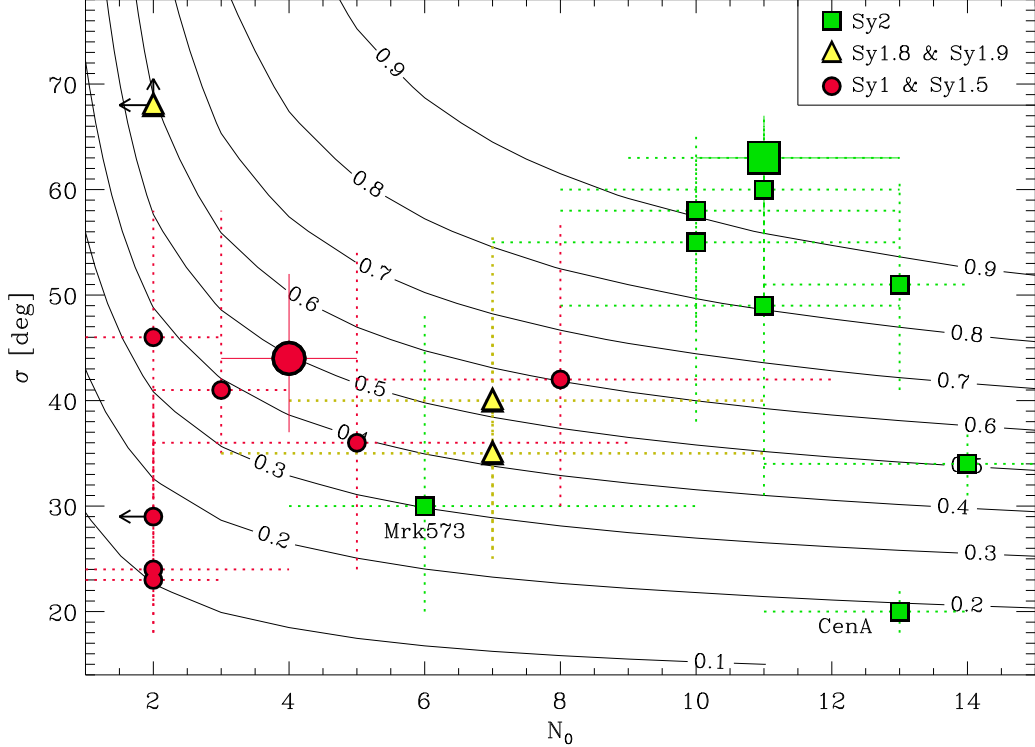


FIG. 11.— σ versus N_0 for the individual galaxies. Either median values or upper/lower limits are taken from the fits presented here. Dots correspond to Type-1 Seyferts, triangles to Sy1.8 and Sy1.9, and squares to Sy2. Error bars indicate 68% confidence level around the median. Note the segregation between Seyfert types, indicating the intrinsic difference between their tori in terms of covering factor (indicated in contours). The big dot and square correspond to the average σ and N_0 values for Sy1 and Sy2 from Table 10.

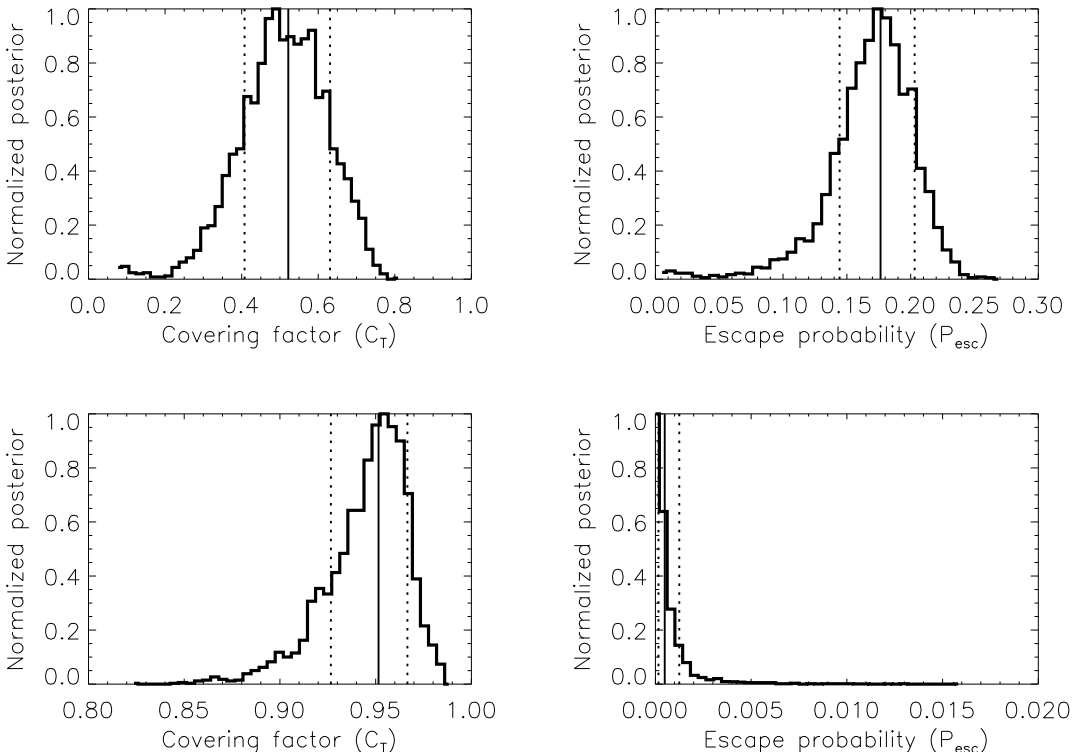


FIG. 12.—Joint posterior distributions of the torus covering factor (left panels) and escape probability (right panels) for Sy1 (top) and Sy2 galaxies (bottom). The values of the Kullback-Leibler divergence obtained from the comparison between Sy1 and Sy2 are $KLD=28$ for of the torus properties on the AGN luminosity consider- ing a broader luminosity range is further investigated in

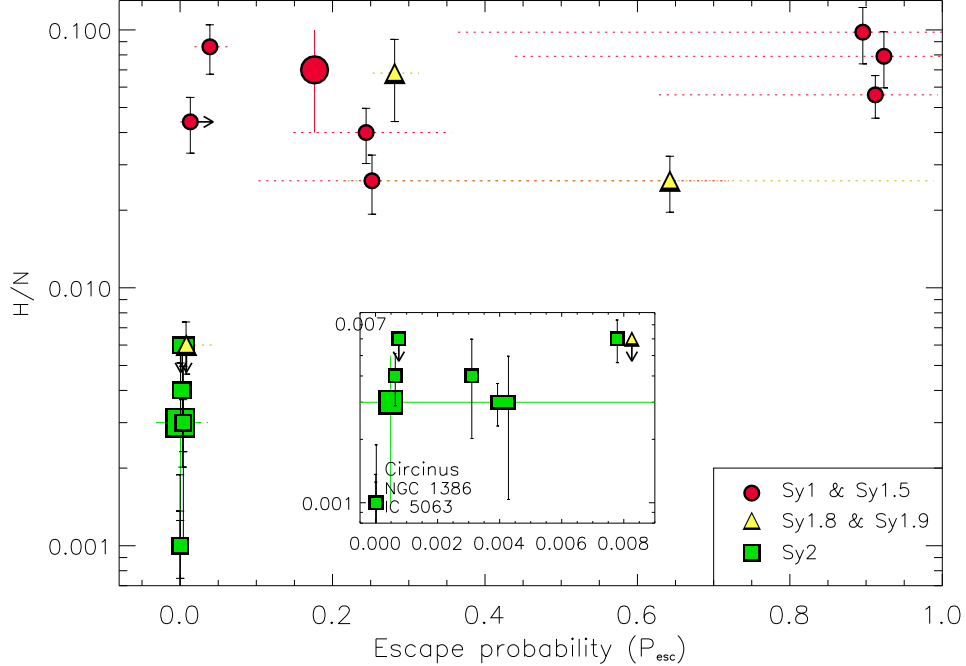


FIG. 13.— H/N versus P_{esc} . Lower values of N_0 , σ , and i result in higher P_{esc} , resulting in higher NIR-to-MIR ratios. The inset shows an amplification of the region occupied by the Sy2. Symbols are the same as in Figure 11. The big dot and square correspond to the median values of P_{esc} for Sy1 and Sy2 from Figure 12, and to the H/N values of the Sy1 and Sy2 average templates (Table 6).

TABLE 11
BOLOMETRIC LUMINOSITY PREDICTIONS

Galaxy	L_{bol}^{AGN}	$L_{bol}^{tor}/L_{bol}^{AGN}$	R_o (pc)	L_{Xbol}^{AGN}	$L_{Xbol}^{AGN}/L_{bol}^{AGN}$	Ref.
NGC 1097	$2.4 \pm 0.8 \times 10^{42}$	0.4 ± 0.1	0.4 ± 0.1	1.0×10^{42}	0.4	a
NGC 1566	$5.9 \pm 1.3 \times 10^{42}$	0.4 ± 0.1	0.6 ± 0.2	6.3×10^{42}	1.1	b
NGC 6221	$6.2 \pm 1.3 \times 10^{42}$	0.7 ± 0.5	0.7 ± 0.3	1.3×10^{43}	2.1	c
NGC 6814	$8.1 \pm 2.4 \times 10^{42}$	0.4 ± 0.2	0.7 ± 0.3	2.7×10^{43}	3.3	d
NGC 7469	$3.7 \pm 0.8 \times 10^{44}$	0.5 ± 0.1	5 ± 1	3.4×10^{44}	0.9	e
NGC 3227	$1.3 \pm 1.3 \times 10^{43}$	0.7 ± 0.5	0.9 ± 0.4	3.8×10^{43}	2.9	f
NGC 4151	$4.6 \pm 1.5 \times 10^{43}$	0.5 ± 0.1	1.4 ± 0.6	1.7×10^{44}	3.7	g

REFERENCES. — (a) Terashima et al. (2002); (b) Levenson et al. (2009); (c) Levenson et al. (2001); (d) Gandhi et al. (2009); (e) Nandra et al. (2007); (f) Lamer et al. (2003); (g) Beckmann et al. (2005).

NOTE. — Bolometric luminosities corresponding to the AGN luminosity (L_{bol}^{AGN} ; in erg s^{-1}). Columns 3 and 4 correspond to the RE ($L_{bol}^{tor}/L_{bol}^{AGN}$) and the outer radius of the torus calculated using L_{bol}^{AGN} and Y . Absorption-corrected 2–10 keV X-ray luminosities are taken from the literature (references below). L_{Xbol}^{AGN} (erg s^{-1}) is derived from $20 \times L_X^{AGN}$.

Alonso-Herrero et al. (2011).

Figure 14 shows that there is a correlation between RE and the torus covering factor for the galaxies in our sample. The larger C_T the more efficient reprocessor. Type-2 tori have in general larger RE than those of Type-1, with the exceptions of Centaurus A and Mrk 573. Despite the relatively small sample, Figure 14 shows a segregation between Sy1 and Sy2 galaxies in terms of reprocessing efficiency and covering factor.

If all Seyfert nuclei are identical, as the unified model predicts, only the viewing angle should determine the classification, not the properties of the torus itself. While our results are limited by the small sample analyzed, they suggest instead that the Type-1/Type-2 classification depends on the torus intrinsic properties rather than in the mere torus inclination.

The bolometric luminosity of the intrinsic AGN derived from the fits (L_{bol}^{AGN} ; column 2 in Table 11) can be directly compared with those from the absorption-corrected 2–10 keV luminosities compiled from the literature (L_{Xbol}^{AGN} ; column 6 in Table 11), which is an effective proxy for the AGN bolometric luminosity (Elvis et al. 1994). To obtain L_{Xbol}^{AGN} from the intrinsic 2–10 keV values we applied a bolometric correction factor of 20 (Elvis et al. 1994).

We find similar values of L_{Xbol}^{AGN} and L_{bol}^{AGN} for all the Sy1 (see Table 11). In the case of NGC 1097, we expect to have some contamination from the nuclear starburst (see Section 5.2.1 and Mason et al. 2007). Thus, if the L_{Xbol}^{AGN} value represents the AGN contribution-only, L_{bol}^{AGN} may be overestimated because of the starburst contribution,

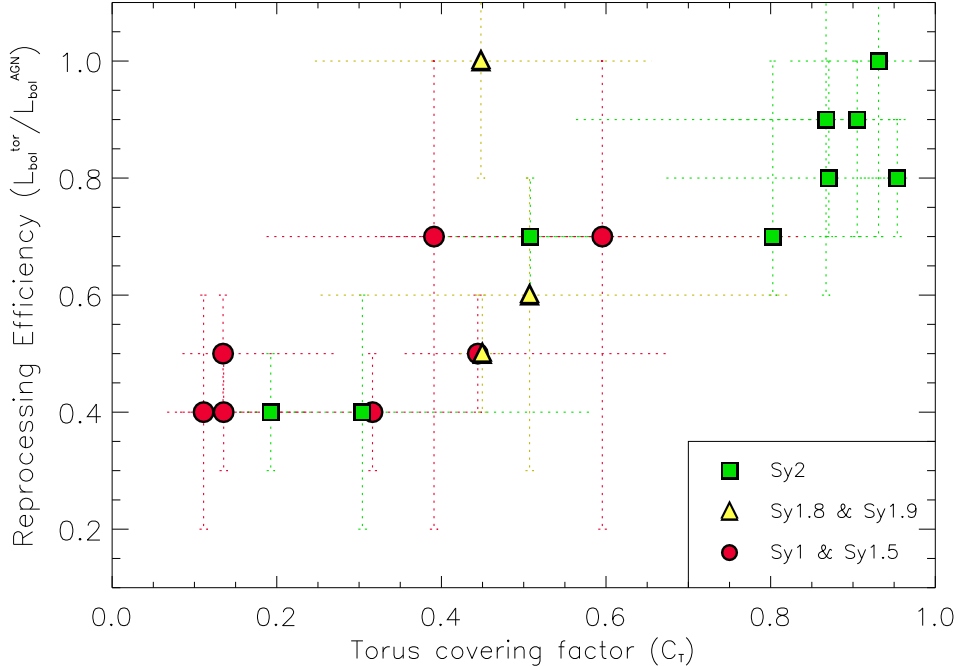


FIG. 14.— Reprocessing efficiency versus torus covering factor for the individual galaxies. Higher values of C_T translate into more efficient reprocessors. In general, Type-2 tori are more efficient than Type-1 tori, with the exceptions of Centaurus A and Mrk 573. Symbols are the same as in Figure 11.

thus resulting in a low ratio between the two measurements. The good agreement with the observational X-ray measurements reinforces the results from our SED modelling. The same comparison with X-ray data for Sy2 and intermediate-type Seyferts is shown in Table B3 in Appendix B.

6.3. Torus Size

In general, the IR SED fitting does not constrain the size of the torus (Y) as well as other model parameters (see Section 5.3 in RA09). The NIR and MIR observations are sensitive to the warm dust (located within ~ 10 pc of the nucleus), which depends on the combination of model parameters N_0 , q , and Y (Thompson et al. 2009). FIR observations would be more sensitive to the torus extent independently. However, the fits performed here for Type-1 and Type-2 Seyferts are consistent with a small torus size, confined to scales of less than 6 pc (see below).

Uniform density models require the dusty torus to extend over large dimensions, to provide cool dust that produces the IR emission (e.g., Granato & Danese 1994). In contrast, in a clumpy distribution, different dust temperatures can coexist at the same distance, including cool dust at small radii (Nenkova et al. 2002), so large tori, which are inconsistent with imaging and interferometry results, are not necessary. Indeed, for the Seyfert galaxies considered here, we found Y ranging from 10 to 25 (see Table 8), showing that small tori can account for the observed IR nuclear emission.

The outer size of the torus scales with the AGN bolometric luminosity: $R_o = YR_d$, so assuming a dust sublimation temperature of 1500 K, $R_o = 0.4 Y (L_{bol}^{AGN}/10^{45})^{0.5}$ pc. We derived R_o posterior distributions from those of L_{bol}^{AGN} and Y and find that all tori in our sample have outer radii smaller than 6 pc (Ta-

bles 11 and B3), in agreement with MIR direct imaging of nearby Seyferts (Packham et al. 2005; Radomski et al. 2008) and also interferometric observations (Jaffe et al. 2004; Tristram et al. 2007; Meisenheimer et al. 2007; Raban et al. 2009).

For example, the estimated outer radius for NGC 1097 ($R_o = 0.4 \pm 0.1$ pc) is in agreement with the value derived from NIR NACO/VLT observations (Prieto et al. 2005), which placed the radius of the central compact source in $r < 5$ pc. Mason et al. (2007) also derived an upper limit of 19 pc for the size of the unresolved component from the MIR images employed in this work for NGC 1097. For the case of NGC 7469, for which we derive $R_o = 5 \pm 1$ pc, Tristram et al. (2009) reported an estimation of the size of the dust distribution of 10 pc, based on MIDI/VLT interferometric observations, although compromised by the high level of noise and the lack of fringes.

7. CONCLUSIONS

We present new subarcsecond resolution MIR imaging data at 8.7 and 18.3 μm for the three Type-1 Seyfert galaxies NGC 6221, NGC 6814, and NGC 7469. NGC 7469 and NGC 6221 appear extended, with part of this extended emission associated with emitting-dust heated by star formation. On the contrary, NGC 6814 lacks of any extended emission. Nuclear MIR and NIR fluxes for the three galaxies as well as for NGC 1566, NGC 1097, NGC 3227, and NGC 4151 are reported. We construct nuclear SEDs that the AGN dominates and fit them with clumpy torus models and a Bayesian approach to derive torus parameters. The main results of this work for the individual Sy1 galaxies and from the comparison with the Sy2 and intermediate-type Seyferts in RA09 are summarized as follows:

- We derived an average Type-1 Seyfert template from the individual Sy1 SEDs, which is flatter

(mean IR slope $\alpha_{IR} = 1.7 \pm 0.3$) than the Type-2 mean SED presented in RA09 ($\alpha_{IR} = 3.1 \pm 0.9$).

- The NIR-to-MIR flux ratios measured from the individual SEDs are larger for Sy1 (0.07 ± 0.03) than for Sy2 (0.003 ± 0.002). Indeed, the distributions of NIR-to-MIR values are significantly different between the two types at the 100% confidence level.
- The interpolated version of the clumpy models of Nenkova et al. (2008a,b) employed here successfully reproduces the nuclear IR SEDs of Type-1 Seyferts with compatible results among them. Consequently, the observed nuclear IR emission of these galaxies can be accounted for by dust heated by the central engine and direct AGN emission.
- We derive joint posterior distributions for Sy1 and Sy2 and find that the differences in N_0 , τ_V , and σ between Type-1 and Type-2 tori are significant according to the Kullback-Leibler divergence and the lack of overlap between their 1-sigma confidence intervals.
- We find that Sy1 tori are narrower and have fewer clouds than those of Sy2. Additionally, the optical depth of the clouds in Sy1 tori is larger than in Sy2.
- There is not a clear trend in the values of the inclination angle of the torus for Sy1 and Sy2 (slightly larger values are found for Sy2).
- The larger the covering factor of the torus, the smaller the likelihood of intercepting a cloud along

a LOS. In our sample, Seyfert 2 tori have larger covering factors and smaller escape probabilities than those of Seyfert 1.

- Despite the limited number of galaxies considered, we find that Type-2 tori are in general more efficient reprocessors than those of Type-1. Indeed, there is a correlation between the reprocessing efficiency and the torus covering factor.
- For the Seyfert galaxies studied here, we find that tori with outer radii smaller than 6 pc can account for the observed NIR/MIR nuclear emission, in agreement with MIR interferometric observations.

Summarizing, we find tantalizing evidence, albeit for a small sample of Seyfert galaxies and under the clumpy torus hypothesis, that the classification as a Type-1 and Type-2 depends more on the intrinsic properties of the torus than on its mere inclination towards us.

APPENDIX

FITTING RESULTS FOR SY1 GALAXIES

Here we include the posterior distributions of the Sy1 galaxies NGC 1566, NGC 6221, NGC 6814, NGC 7469, NGC 3227, and NGC 4151 (Figures A1 to A6).

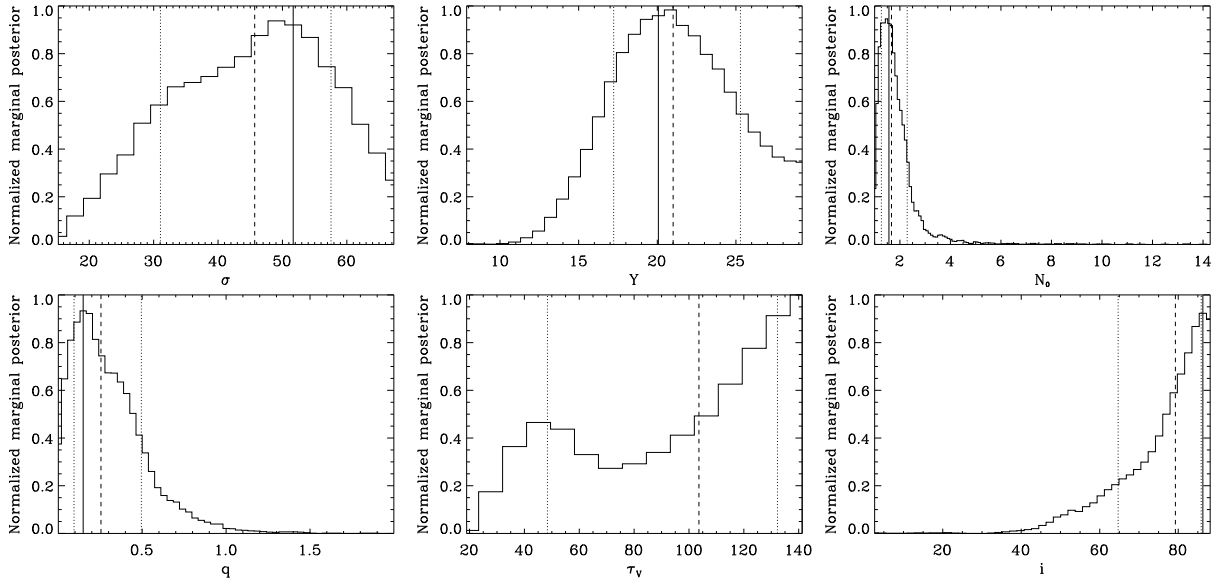


FIG. A1.— Same as in Figure 8, but for the galaxy NGC 1566.

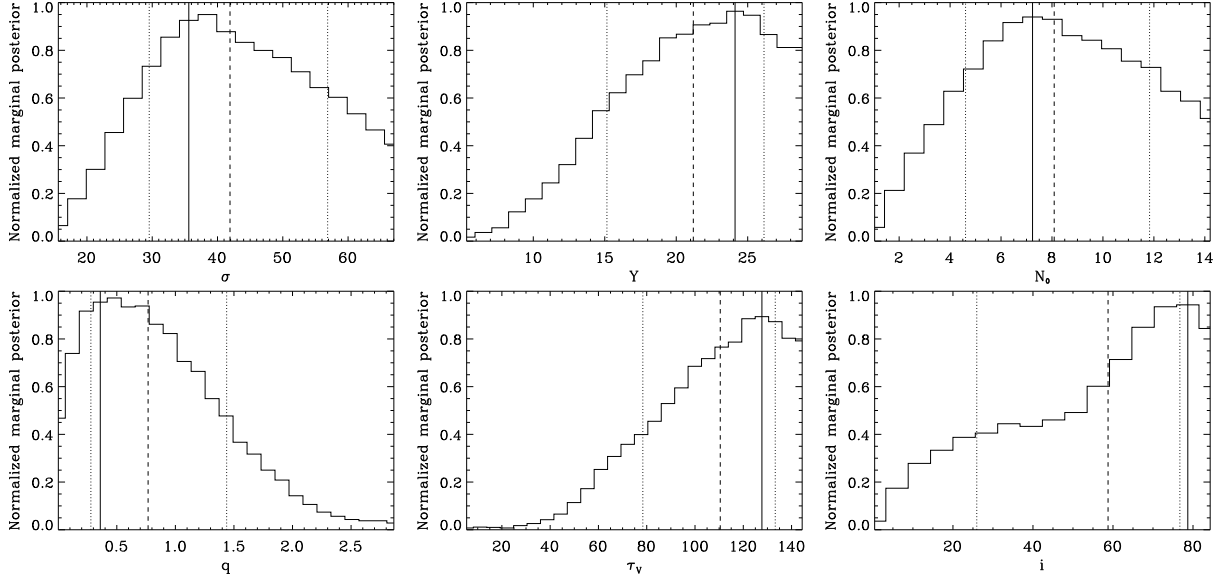


FIG. A2.— Same as in Figure 8, but for the galaxy NGC 6221.

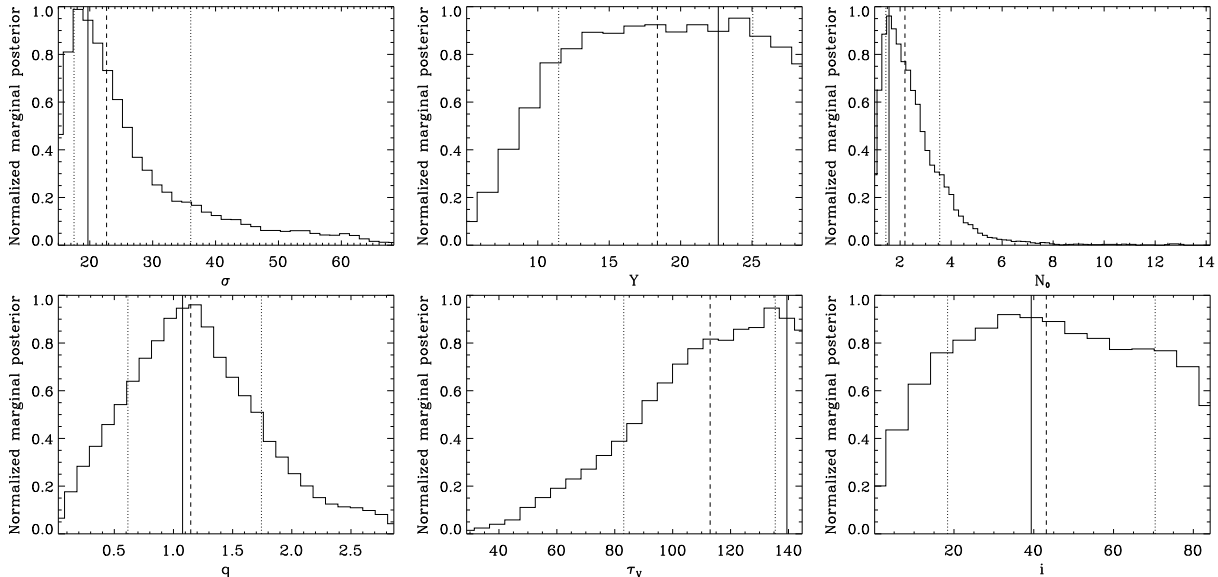


FIG. A3.— Same as in Figure 8, but for the galaxy NGC 6814.

TABLE A1
VISIR MIR FLUXES FROM THE LITERATURE FOR THE SY1 GALAXIES

Galaxy	Flux Density (mJy)	Filter(s)	Reference(s)
NGC 1097	$28 \pm 7, 49 \pm 12$	12.27, 18.72	B1,B2
NGC 1566	$63 \pm 9, 128 \pm 32$	11.88, 18.72	B2
NGC 6814	$99 \pm 6, 96 \pm 6$	11.25,13.04	B3
NGC 7469	$448 \pm 16, 595 \pm 18, 630 \pm 17, 1270 \pm 317$	10.49,12.27,13.04,18.72	B1,B4,B2
NGC 3227	$180 \pm 11, 320 \pm 22$	8.99, 11.88	B4

REFERENCES. — (B1) Horst et al. (2008); (B2) Reunanen et al. (2010); (B3) Gandhi et al. (2009); (B4) Hönig et al. (2010)

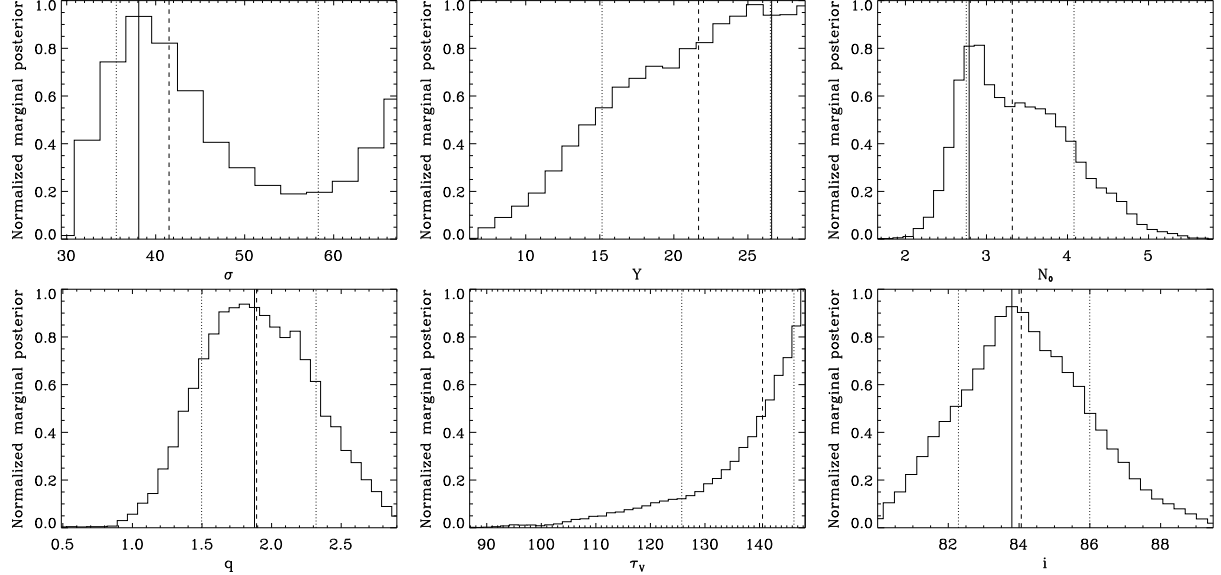


FIG. A4.— Same as in Figure 8, but for the galaxy NGC 7469.

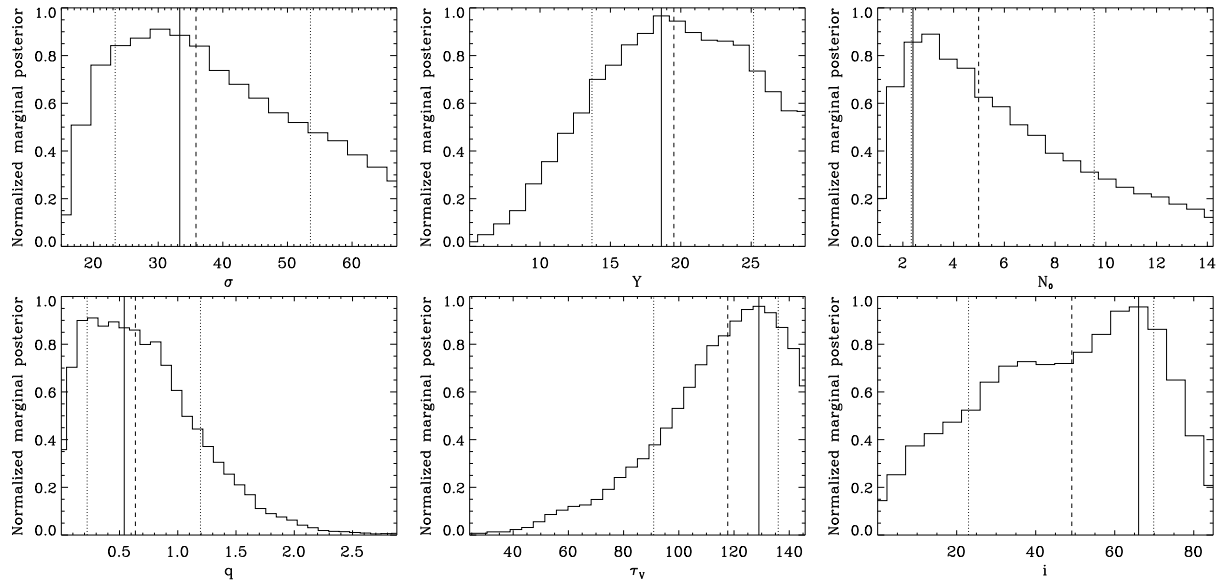


FIG. A5.— Same as in Figure 8, but for the galaxy NGC 3227.

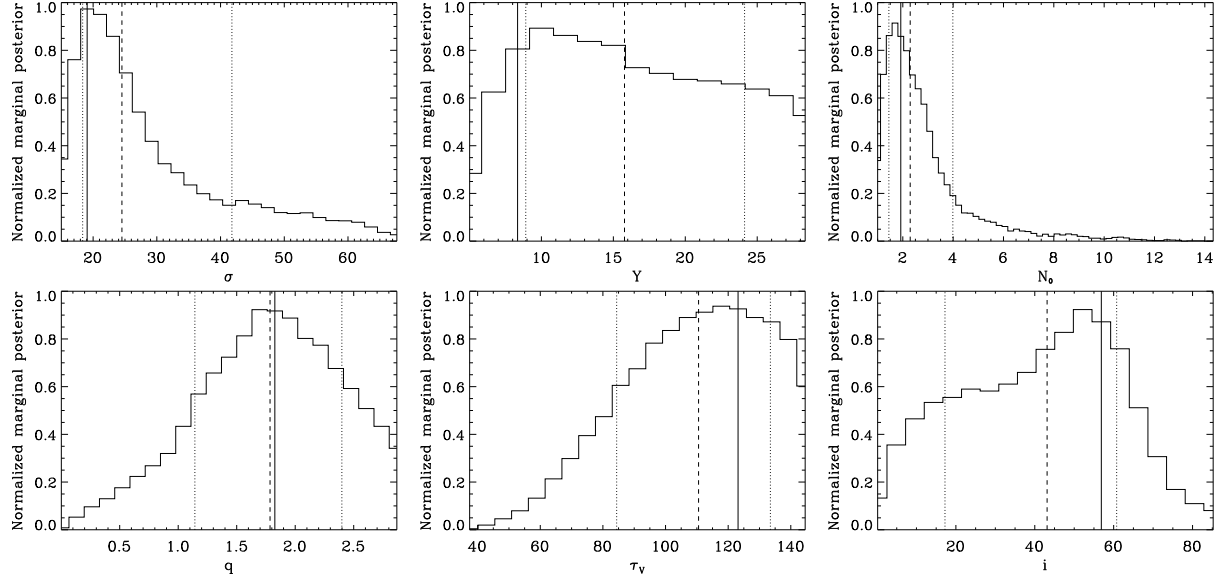


FIG. A6.— Same as in Figure 8, but for the galaxy NGC 4151.

TABLE B1
NIR AND MIR FLUXES FROM THE LITERATURE FOR SY2 AND INTERMEDIATE-TYPE SEYFERTS

Galaxy	Seyfert	Flux Density (mJy)	Filter(s)	Reference(s)
CenA	2	1.3±0.1, 4.5±0.3, 34±2, 200±40 643±27, 947±29, 1100±100, 1451±73, 2300±575	NACO J,H,K,L' VISIR 10.49,11.25,11.88,12.27,18.72	A1 B1,B2
Circinus	2	1.6±0.2, 4.8±0.7, 19±2, 31±3, 380±38, 1900±190	F160W, NACO J,K,2.42,L,M	A2
IC 5063	2	0.3±0.1, 4.77±0.95 609±22, 727±25, 925±25, 1036±56	F160W, F222M VISIR 10.49,11.25,11.88,12.27	A3, A10 B3
Mrk 573	2	0.15±0.06, 0.54±0.04, 3.2±0.6, 18.8±3.8, 41.3±8.3	F110W,F160W, NSFCam K',L,M	A4
NGC 1386	2	0.2±0.1	F160W	A3
NGC 1808	2	15.5±4.5, 30.5±8.5, 27.5±10.5	ISAAC J,Ks,L'	A5
NGC 3081	2	0.22±0.13 138±11	F160W VISIR 13.04	A3 B4
NGC 3281	2	1.3±0.2, 7.7±0.8, 103±9, 207±25 481±24, 1016±52	IRAC-1 H,K, IRCAM3 L',M VISIR 11.25,13.04	A6 B4
NGC 4388	2	0.06±0.02, 0.71±0.28, 40±8 147±11, 375±28	F110W,F160W, NSFCam L	A4 B4
NGC 7172	2	<0.4, 3.4±0.7, 30±6, 61±12 165±27	IRCAM3 H,K,L',M VISIR 12.27	A7 B1
NGC 7582	2	11±1, 18±2, 96±10, 110±11, 142±21 236±27, 550±130	F160W, NACO 2.06,L,4.05, ISAAC M VISIR 8.99, 18.72	B2,A8 B3,B2
NGC 1365	1.8	8.3±0.8	F160W	A9
NGC 2992	1.9	<1, 2.8±0.6, 22.7±4.5, 35.7±7.1 312±31	IRCAM3 H,K,L',M VISIR 11.25	A7 B5
NGC 5506	1.9	13±1, 53±1, 80±1, 290±10, 351±29 900±100, 1400±350	NACO J,H,K,L', NSFCam M VISIR 11.88, 18.72	B2,A11 B2

REFERENCES. — (A1) Meisenheimer et al. (2007); (A2) Prieto et al. (2004); (A3) Quillen et al. (2001); (A4) Alonso-Herrero et al. (2003); (A5) Galliano & Alloin (2008); (A6) Simpson (1998); (A7) Alonso-Herrero et al. (2001); (A8) Prieto et al. (2002); (A9) Carollo et al. (2002); (A10) Kulkarni et al. (1998); (A11) Ward et al. (1987); (B1) Horst et al. (2008); (B2) Prieto et al. (2010); (B3) Höning et al. (2010); (B4) Gandhi et al. (2009); (B5) Haas et al. (2007)

NOTE. — Ground-based instruments and telescopes are: NACO and ISAAC on the 8 m VLT, NSFCam on the 3 m NASA IRTF, IRCAM3 on the 3.8 m UKIRT, and IRAC-1 on the 2.2 m ESO telescope. Measurements in the F110W, F160W, and F222M filters are from NICMOS on HST.

TABLE B2
PARAMETERS FROM THE FITS FOR SY2 AND INTERMEDIATE-TYPE SEYFERTS

Galaxy	σ	Y	N_0	q	i	τ_V	A_V^{LOS}
	Med	Mode	Med	Med	Med	Med	Med
CenA	20±2	20	13±2	13	13±1	15	0.4±0.2
Circinus	63±4	68	20±6	27	11±2	11	2.6±0.2
IC 5063	51±10	56	12±4	10	13±1	14	0.8±0.3
Mrk 573	30±18	23	17±8	25	6±4	5	0.9±0.8
NGC 1386	49±18	52	17±8	17	11±2	13	1.5±0.8
NGC 1808	26±12	20	18±7	18	8±4	12	1.3±0.9
NGC 3081	55±17	61	18±8	22	10±3	12	1.4±0.9
NGC 3281	34±3	34	10±2	9	14±1	15	<0.2
NGC 4388	60±6	67	20±5	22	11±2	14	0.5±0.6
NGC 7172	58±10	66	14±9	8	10±3	9	1.9±0.7
NGC 7582	34±20	23	18±8	18	3±2	2	2.3±0.6
NGC 1365	35±14	32	18±7	22	7±4	4	1.1±0.8
NGC 2992	40±14	28	18±7	24	7±4	5	0.9±1.0
NGC 5506	>68	69	23±4	26	<2	1	>2.9

NOTE. — For the galaxies Circinus, Mrk 573, NGC 1386, and NGC 5506 the i parameter has been introduced as a Gaussian prior into the computations, centered at 85° with a width of 2° , based on other observations. Probability distributions presenting a single tail have been characterized with the mode and upper/lower limits at 68% confidence. Sy1.8 and Sy1.9 have been fitted with the geometry corresponding to torus emission-only.

^aThe inclination angle of the torus was introduced as a uniform prior $i=[60^\circ, 90^\circ]$ following Storchi-Bergmann et al. (1992).

FITTING RESULTS FOR SY2 AND INTERMEDIATE-TYPE SEYFERT GALAXIES

Here we include the results of the fits of the intermediate-type Seyferts and the Sy2 galaxies in RA09 (Figures B1 and B2) using the data reported in Table B1 and the most up-to-date version of the Nenkova et al. (2008a,b) models (see erratum Nenkova et al. 2010). The resulting model parameters for the individual galaxies are shown in Tables B2 and B3. In Figure B3 we show the posterior distributions from the fit of Centaurus A (see the electronic edition of the Journal for the rest of the Sy2 and intermediate-type Seyferts posteriors.).

As mentioned in Section 5.2.2, the results presented in this Appendix are compatible in general with those presented in RA09 at the 1-sigma level. For the majority of the galaxies, we have included IR data from recent publications.

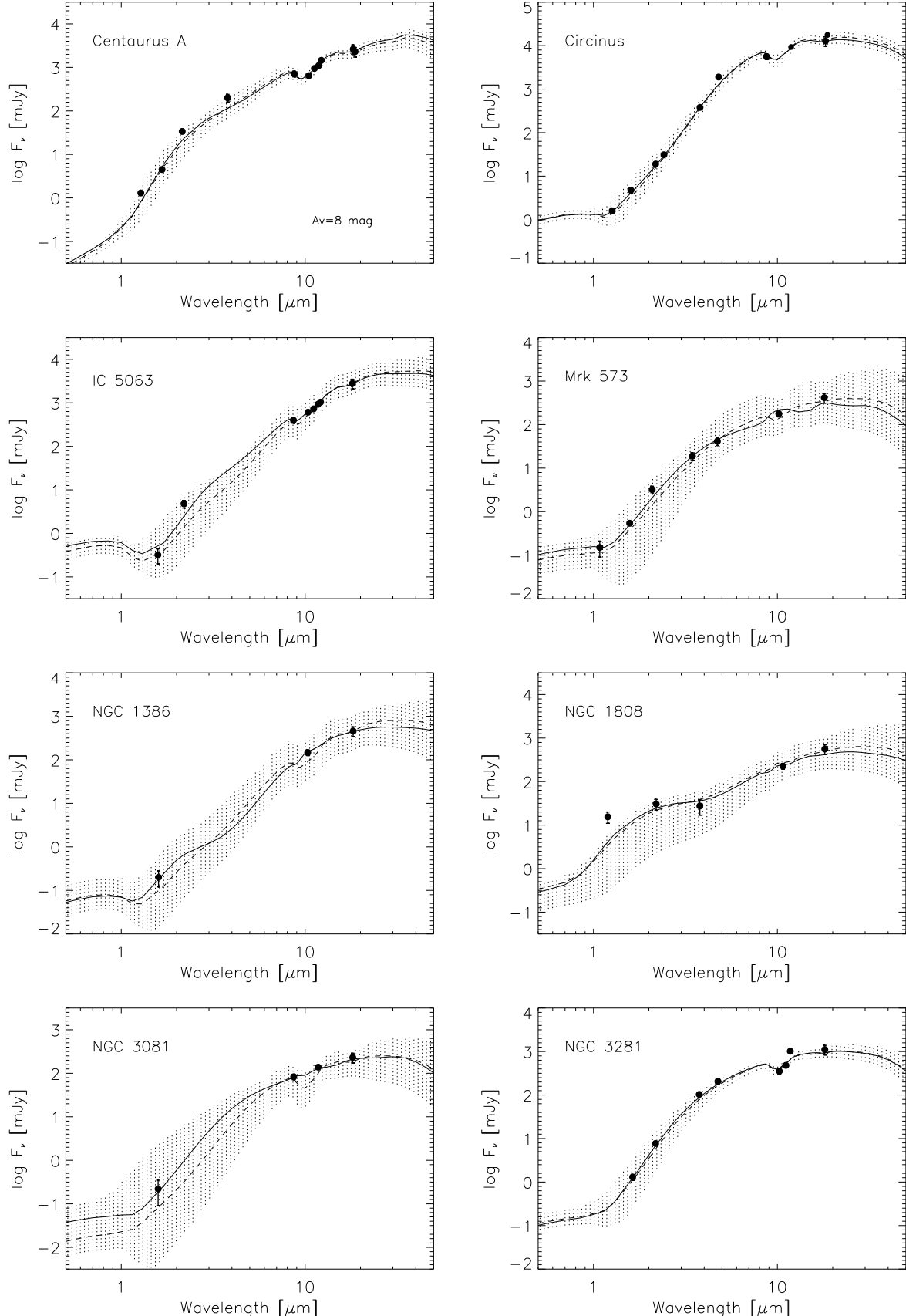


FIG. B1.— Same as in Figure 6, but for the Sy2 galaxies Centaurus A, Circinus, IC 5063, Mrk 573, NGC 1386, NGC 1808, NGC 3081, and NGC 3281.

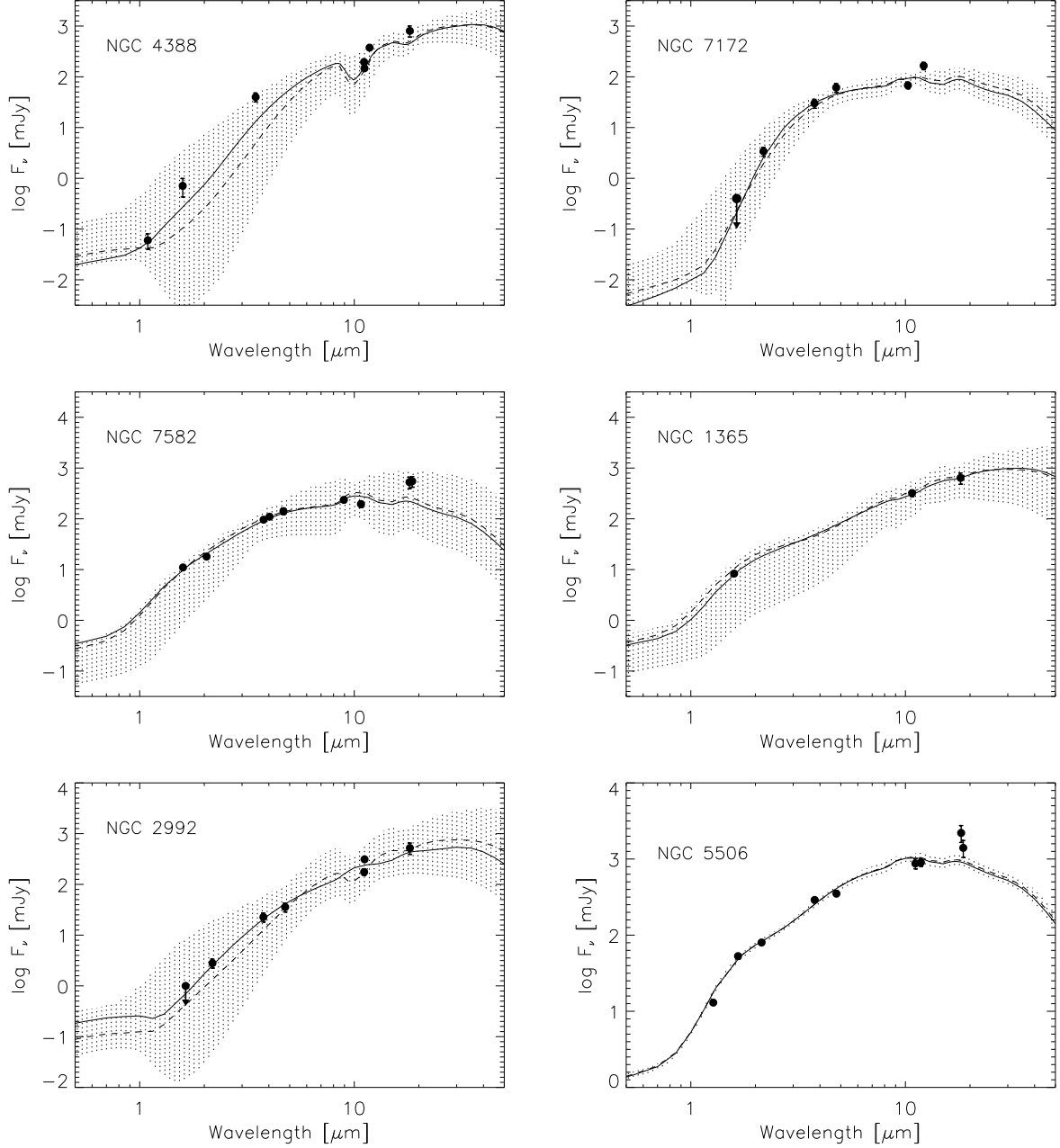


FIG. B2.— Same as in Figure 6, but for the Sy2 galaxies NGC 4388, NGC 7172, and NGC 7582; the Sy1.8 NGC 1365, and the Sy1.9 galaxies NGC 2992 and NGC 5506.

In particular, the use of VISIR MIR data have been key in predicting the silicate feature in absorption in the case of Centaurus A²⁰ and NGC 3281, and in emission in NGC 3227.

In the case of Centaurus A, the fit presented in RA09 predicted the silicate feature in emission, in clear contradiction with MIR spectroscopic data (Siebenmorgen et al. 2004; Meisenheimer et al. 2007). By including the VISIR data for this galaxy, the fitted models predict a broad silicate feature, in agreement with the observations. Additionally, we have also introduced the inclination angle of the torus as a gaussian prior centred in 70° as inferred from the inclination of the inner radio jet of Centaurus A (Tingay et al. 1998). This value is also coincident with the 66° inclination angle of the obscuring structure derived from MIR interferometric observations (Burtscher et al. 2010).

For the Sy2 galaxy NGC 3281 we also have considered a uniform prior in the range $[60^\circ, 90^\circ]$ for the inclination angle of the torus, based on the inclination of the ionization cone axis derived in Storchi-Bergmann et al. (1992) from optical imaging and spectroscopic observations, which implies a nearly edge-on orientation of the obscuring structure.

²⁰ In order to account for the extinction caused by the dust lane of $A_V \sim 7\text{-}8$ mag in Centaurus A, we have considered the Chiar & Tielens (2006) law in the fit fixing $A_V=8$ mag.

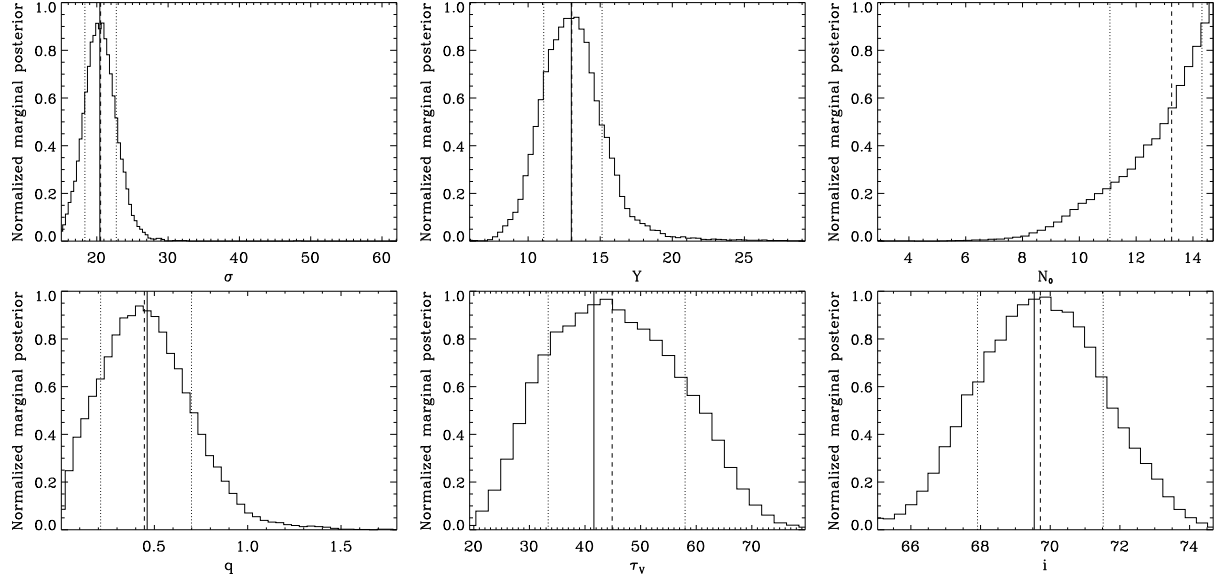


FIG. B3.— Same as in Figure 8, but for the galaxy Centaurus A. See the electronic edition of the Journal for the rest of the Sy2 and intermediate-type Seyferts.

TABLE B3
BOLOMETRIC LUMINOSITY PREDICTIONS

Galaxy	L_{bol}^{AGN}	$L_{bol}^{tor}/L_{bol}^{AGN}$	R_o (pc)	L_{Xbol}^{AGN}	$L_{Xbol}^{AGN}/L_{bol}^{AGN}$	Ref.
Centaurus A	$4.7 \pm 0.8 \times 10^{42}$	0.4 ± 0.1	0.4 ± 0.1	1.3×10^{43}	3	a
Circinus	$1.0 \pm 0.2 \times 10^{43}$	0.8 ± 0.1	0.8 ± 0.3	1.2×10^{43}	1.2	b
IC 5063	$2.7 \pm 1.2 \times 10^{44}$	0.8 ± 0.1	2.5 ± 1.3	1.7×10^{44}	0.6	c
Mrk 573	$1.5 \pm 0.1 \times 10^{44}$	0.4 ± 0.2	2.8 ± 1.2	4.4×10^{44}	3	d
NGC 1386	$2.8 \pm 0.6 \times 10^{42}$	0.7 ± 0.1	0.4 ± 0.2	1.3×10^{43}	5	e
NGC 1808	$3.1 \pm 0.4 \times 10^{42}$	0.8 ± 0.4	0.4 ± 0.2	2.2×10^{41}	0.1	f
NGC 3081	$7.6 \pm 4.6 \times 10^{42}$	0.9 ± 0.3	0.7 ± 0.3	1.0×10^{44}	13	d
NGC 3281	$1.1 \pm 0.9 \times 10^{44}$	0.7 ± 0.1	1.3 ± 0.3	3.0×10^{44}	3	g
NGC 4388	$2.3 \pm 1.1 \times 10^{43}$	1.0 ± 0.3	1.3 ± 0.4	1.5×10^{44}	6	h
NGC 7172	$8.4 \pm 1.6 \times 10^{42}$	0.9 ± 0.2	0.5 ± 0.3	1.1×10^{44}	13	i
NGC 7582	$1.4 \pm 0.4 \times 10^{43}$	0.6 ± 0.1	0.8 ± 0.4	9.8×10^{43}	7	j
NGC 1365	$8.1 \pm 2.9 \times 10^{42}$	1.0 ± 0.3	0.7 ± 0.3	3.0×10^{43}	4	k
NGC 2992	$3.0 \pm 2.5 \times 10^{43}$	0.6 ± 0.2	1.3 ± 0.7	3.0×10^{43}	1.0	l
NGC 5506	$9.3 \pm 0.2 \times 10^{43}$	0.5 ± 0.1	2.9 ± 0.7	2.2×10^{44}	2	m

REFERENCES. — (a) Markowitz et al. (2007); (b) Soldi et al. (2005); (c) Turner et al. (1997); (d) RA09; (e) Levenson et al. (2006); (f) Jiménez-Bailón et al. (2005); (g) Vignali & Comastri (2002); (h) Elvis et al. (2004); (i) Awaki et al. (2006); (j) Turner et al. (2000); (k) Risaliti et al. (2005); (l) Yaqoob et al. (2007); (m) Lamer et al. (2000); (n) Lamer et al. (2003); (o) Beckmann et al. (2005).

NOTE. — Same as in Table 11, but for the Sy2 and intermediate-type Seyfert galaxies in RA09.

C.R.A. and J.R.E. acknowledge the Spanish Ministry of Science and Innovation (MICINN) through Consolider-Ingenio 2010 Program grant CSD2006-00070: First Science with the GTC (<http://www.iac.es/consolider-ingenio-gtc/>). C.R.A. acknowledges financial support from STFC PDRA (ST/G001758/1). A.A.H acknowledges support from the Spanish Plan Nacional del Espacio under grant ESP2007-65475-C02-01 and Plan Nacional de Astronomía y Astrofísica under grant AYA2009-05705-E. A.A.R. acknowledges the Spanish Ministry of Science and Innovation (MICINN) through project AYA2007-63881. A.M.P.G. acknowledges the Spanish Ministry of Science and Innovation (MICINN) through project AYA2008-06311-C02-01. C.P. acknowledges support from the NSF under grant number 0904421.

This work is based on observations obtained at the Gemini Observatory, which is operated by the Association of Universities for Research in Astronomy, Inc., under a cooperative agreement with the NSF on behalf of the Gemini partnership: the National Science Foundation (United States), the Science and Technology Facilities Council (United Kingdom), the National Research Council (Canada), CONICYT (Chile), the Australian Research Council (Australia), Ministério da Ciência e Tecnologia (Brazil), and Ministerio de Ciencia, Tecnología e Innovación Productiva (Argentina). The Gemini programs under which the data were obtained are GS-2005B-DD, GS-2005B-Q-29, and GS-2009B-Q-43.

This work is based on observations made with the NASA/ESA Hubble Space Telescope, and obtained from the Hubble Legacy Archive, which is a collaboration between the Space Telescope Science Institute (STScI/NASA), the Space Telescope European Coordinating Facility (ST-ECF/ESA) and the Canadian Astronomy Data Centre (CADC/NRC/CSA).

This research has made use of the NASA/IPAC Extragalactic Database (NED) which is operated by the Jet Propulsion Laboratory, California Institute of Technology, under contract with the National Aeronautics and Space Administration.

We finally acknowledge useful comments from the anonymous referee.

REFERENCES

- Alonso-Herrero, A., et al. 2011, ApJ, submitted
 Alonso-Herrero, A., Colina, L., Packham, C., Díaz-Santos, T., Rieke, G. H., Radomski, J. T., & Telesco, C. M. 2006, ApJ, 652, L83
 Alonso-Herrero, A., Quillen, A. C., Rieke, G. H., Ivanov, V. D., & Efstathiou, A. 2003, AJ, 126, 81
 Alonso-Herrero, A., Quillen, A. C., Simpson, C., Efstathiou, A., & Ward, M. J. 2001, AJ, 121, 1369
 Alonso-Herrero, A., Ward, M. J., & Kotilainen, J. K. 1996, MNRAS, 278, 902
 Antonucci, R. R. J. 1993, ARA&A, 31, 473
 Antonucci, R. R. J., & Miller, J. 1985, ApJ, 297, 621
 Asensio Ramos, A. & Ramos Almeida, C. 2009, ApJ, 696, 2075
 Awaki, H., Murakami, H., Ogawa, Y., & Leighly, K. M. 2006, ApJ, 645, 928
 Ayani, K., & Maehara, H. 1991, PASJ, 43, L1
 Barvainis, R. 1987, ApJ, 320, 537
 Beckmann, V., Shrader, C. R., Gehrels, N., Sokli, S., Lubinski, P., Zdziarski, A. A., Petrucci, P.-O., & Malzac, J. 2005, ApJ, 634, 939
 Burtscher, L., Meisenheimer, K., Jaffe, W., Tristram, K. R. W., & Rottgering, H. J. A. 2010, PASA, 27, 490
 Calzetti, D., et al. 2005, ApJ, 633, 871
 Carollo, C. M., Stiavelli, M., Seigar, M., de Zeeuw, P. T., & Dejonghe, H. 2002, AJ, 123, 159
 Chiar, J. E. & Tielens, A. G. G. M. 2006, ApJ, 637, 774
 Colina, L., Alberdi, A., Torrelles, J. M., Panagia, N., & Wilson, A. S. 2001, ApJ, 553, L19
 Díaz-Santos, T., Alonso-Herrero, A., Colina, L., Ryder, S. D., & Knapen, J. H. 2007, ApJ, 661, 149
 Dulemond, C. P. & van Bemmel, I. M. 2005, A&A, 436, 47
 Edelson, R. A., Malkan, M. A., & Rieke, G. H. 1987, ApJ, 321, 233
 Elitzur, M., & Shlosman, I. 2006, ApJ, 648, L101
 Efstathiou, A., & Rowan-Robinson, M. 1995, MNRAS, 273, 649
 Elvis, M., Risaliti, G., Nicastro, F., Miller, J. M., Fiore, F., & Puccetti, S. 2004, ApJ, 615, L25
 Elvis, M., et al. 1994, ApJS, 95, 1
 Fadda, D., Giuricin, G., Granato, G. L., & Vecchies, D. 1998, ApJ, 496, 117
 Feroz, F., Hobson, M. P., & Bridges, M. 2009, MNRAS, 398, 1601
 Galliano, E. & Alloin, D. 2008, A&A, 487, 519
 Gandhi, P., Horst, H., Smette, A., Höning, S., Comastri, A., Gilli, R., Vignali, C., Duschl, W.
 Garcia, A. 1993, A&AS, 100, 47
 Genzel, R., Weitzel, L., Tacconi-Garman, L. E., Blietz, M., Cameron, M., Krabbe, A., Lutz, D., & Sternberg, A. 1995, ApJ, 444, 129
 Granato, G. L., & Danese, L. 1994, MNRAS, 268, 235
 Granato, G. L., Danese, L., & Franceschini, A. 1997, ApJ, 486, 147
 Haas, M., et al. 2007, A&A, 473, 369
 Heckman, T. M., Beckwith, S., Blitz, L., Skrutskie, M., & Wilson, A. S. 1986, ApJ, 305, 157
 Helou, G., et al. 2004, ApJS, 154, 253
 Hicks, E. K. S., & Malkan, M. A. 2008, ApJS, 174, 31
 Höning, S. F., et al. 2010, A&A, 515, 23
 Höning, S. F., Beckert, T., Ohnaka, K., & Weigelt, G. 2006, A&A, 452, 459
 Horst, H., Duschl, W. J., Gandhi, P., & Smette, A. 2009, A&A, 495, 137
 Horst, H., Gandhi, P., Smette, A., & Duschl, W. J. 2008, A&A, 479, 389
 Jaffe, W., et al. 2004, Nature, 429, 47
 Jiménez-Bailón, E., Santos-Lleó, M., Dahlem, M., Ehle, M., Mass-Hesse, J. M., Guainazzi, M., Heckman, T. M., & Weaver, K. A. 2005, A&A, 442, 861
 Keel, W. C. 1983, ApJ, 269, 466
 Kishimoto, M., Höning, S. F., Beckert, T., & Weigelt, G. 2007, A&A, 476, 713
 Koribalski, B., & Dickey, J. M. 2004, MNRAS, 348, 1255
 Kotilainen, J. K., Ward, M. J., Boisson, C., Depoy, D. L., Smith, M. G., & Bryant, L. R. 1992, MNRAS, 256, 125
 Kriss, G. A., et al. 1990, BAAS, 22, 1280
 Krist, J. 1993, in ASP Conf. Ser. 52, Astronomical Data Analysis Software and Systems II, ed. R. J. Hanish, R. J. V. Brissenden, & J. Barnes (San Francisco, CA:ASP), 536
 Krolik, J. H. & Begelman, M. C. 1988, ApJ, 329, 702
 Kulkarni, V. P., et al. 1998, ApJ, 492, L121
 Kullback, S., & Leibler, A. 1951, Annals Math. Stat., 22, 79
 Lamer, G., Uttley, P., & McHardy, I. M. 2003, MNRAS, 342, L41
 Lamer, G., Uttley, P., & McHardy, I. M. 2000, MNRAS, 319, 949
 Lawrence, A. 1991, MNRAS, 252, 586
 Levenson, N. A., Radomski, J. T., Packham, C., Mason, R. E., Schaefer, J. J., & Telesco, C. M. 2009, ApJ, 703, 390
 Levenson, N. A., Heckman, T. M., Krolik, J. H., Weaver, K. A., Źycki, P. T. 2006, ApJ, 648, 111
 Levenson, N. A., Weaver, K. A., & Heckman, T. M. 2001, ApJS, 133, 269
 Liszt, H. S., & Dickey, J. M. 1995, AJ, 110, 998
 Maiolino, R., Salvati, M., Bassani, L., Dadina, M., della Ceca, R., Matt, G., Risaliti, G., & Zamorani, G. 1998, A&A, 338, 781
 Malkan, M. A., Gorjian, V., & Tam, R. 1998, ApJS, 117, 25
 Markowitz, A., et al. 2007, ApJ, 665, 209
 Mason, R. E., Levenson, N. A., Shi, Y., Packham, C., Gorjian, V., Cleary, K., Rhee, J., & Werner, M. 2009, ApJ, 693, L136

- Mason, R. E., Levenson, N. A., Packham, C., Elitzur, M., Radomski, J., Petric, A. O., & Wright, G. S. 2007, ApJ, 659, 241
- Mason, R. E., Geballe, T. R., Packham, C., Levenson, N. A., Elitzur, M., Fisher, R. S., & Perlman, E. 2006, ApJ, 640, 612
- Meisenheimer, K., et al. 2007, A&A, 471, 453
- Miles, J. W., Houck, J. R., & Hayward, T. L. 1994, ApJ, 425, L37
- Molina, M., et al. 2006, MNRAS, 371, 821
- Mor, R., Netzer, H., & Elitzur, M. 2009, ApJ, 705, 298
- Moran, E. C., Halpern, J.P., & Helfand, D. J. 1996, ApJS, 106, 341
- Mukai, K., Hellier, C., Madejski, G., Patterson, J., & Skillman, D. R. 2003, ApJ, 597, 479
- Mundell, C. G., Holloway, A. J., Pedlar, A., Meaburn, J., Kukula, M. J., & Axon, D. J. 1995, MNRAS, 275, 67
- Nandra, K., O'Neill, P.M., George, I. M., & Reeves, J. N. 2007, MNRAS, 382, 194
- Nenkova, M., Sirocky, M. M., Nikutta, R., Ivezić, Ž., Elitzur, M. 2010, ApJ, 723, 1827
- Nenkova, M., Sirocky, M. M., Ivezić, Ž., & Elitzur, M. 2008, ApJ, 685, 147
- Nenkova, M., Sirocky, M. M., Nikutta, R., Ivezić, Ž., & Elitzur, M. 2008, ApJ, 685, 160
- Nenkova, M., Ivezić, Ž., & Elitzur, M., 2002, ApJ, 570, 9
- Nikutta, R., Elitzur, M., & Lacy, M. 2009, ApJ, 707, 1550
- Osterbrock, D. E. & Martel, A. 1993, ApJ, 414, 5520
- Packham, C., Radomski, J. T., Roche, P. F., Aitken, D. K., Perlman, E., Alonso-Herrero, A., Colina, L., & Telesco, C. M. 2005, ApJ, 618, L17
- Packham, C., Young, S., Hough, J. H., Axon, D. J., & Bailey, J. A. 1997, MNRAS, 288, 375
- Peng, C. Y., Ho, L. C., Impey, C. D., & Rix, H.-W. 2002, AJ, 124, 266
- Phillips, M. M., Pagel, B. E. J., Edmunds, M. G., & Díaz, A. 1984, MNRAS, 210, 701
- Pier, E. A., & Krolik, J. H. 1993, ApJ, 418, 673
- Pier, E. A., & Krolik, J. H. 1992, ApJ, 401, 99
- Prieto, M. A., Reunanen, J., Tristram, K. R. W., Neumayer, N., Fernandez-Ontiveros, J. A., Orienti, M., & Meisenheimer, K. 2010, MNRAS, 402, 724
- Prieto, M. A., Maciejewski, W. & Reunanen, J. 2005, AJ, 130, 1472
- Prieto, M. A., et al. 2004, ApJ, 614, 135
- Prieto, M. A., Reunanen, J., & Kotilainen, J. K. 2002, ApJ, 571, L7
- Quillen, A. C., McDonald, C., Alonso-Herrero, A., Lee, A., Shaked, S., Rieke, M. J., & Rieke, G. H. 2001, ApJ, 547, 129
- Raban, D., Jaffe, W., Röttgering, H., Meisenheimer, K., & Tristram, K. 2009, MNRAS, 394, 1325
- Radomski, J. T., et al. 2008, ApJ, 681, 141
- Radomski, J. T., Piña, R. K., Packham, C., Telesco, C. M., De Buizer, J. M., Fisher, R. S., & Robinson, A. 2003, ApJ, 587, 117
- Radomski, J. T., Piña, R. K., Packham, C., Telesco, C. M., & Tadhunter, C. N. 2002, ApJ, 566, 675
- Ramos Almeida, C., et al. 2009a, ApJ, 702, 1127
- Ramos Almeida, C., Pérez García, A. M., & Acosta-Pulido, J. A. 2009b, ApJ, 694, 1379
- Ramos Almeida, C., Pérez García, A. M., Acosta-Pulido, J. A., & González-Martín, O. 2008, ApJ, 680, L17
- Regan, M. W., & Mulchaey, J. S. 1999, AJ, 117, 2676
- Reunanen, J., Prieto, M. A., & Siebenmorgen, R. 2010, MNRAS, 402, 879
- Rieke, G. H. 1978, ApJ, 226, 550
- Rieke, G. H. & Lebofsky, M. J. 1981, ApJ, 250, 87
- Risaliti, G., Elvis, M., Fabbiano, G., Baldi, A., & Zezas, A. 2005, ApJ, 623, 93
- Risaliti, G., Elvis, M., & Nicastro, F. 2002, ApJ, 571, 234
- Risaliti, G., Maiolino, R., & Salvati, M. 1999, ApJ, 522, 157
- Rodríguez Espinosa, J. M., & Pérez García, A. M. 1997, ApJ, 487, L33
- Rubin, V. C., & Ford, W. K., Jr. 1968, AJ, 73, 861
- Sandage, A., & Bedke, J. 1994, The Carnegie Atlas of Galaxies (Washington, DC: Carnegie Institution of Washington)
- Schartmann, M., Meisenheimer, K., Camenzind, M., Wolf, S., Tristram, K. R. W., & Henning, T. 2008, A&A, 482, 67
- Scoville, N. Z., Evans, A. S., Thompson, R., Rieke, M., Hines, D. C., Low, F. J., Dinshaw, N., Surace, J. A., & Armus, L., 2000, AJ, 119, 991
- Siebenmorgen, R., Krügel, E., & Spoon, H. W. W. 2004, A&A, 414, 123
- Simpson, C. 1998, ApJ, 509, 653
- Soifer, B. T., Bock, J. J., Marsh, K., Neugebauer, G., Matthews, K., Egami, E., & Armus, L. 2003, AJ, 126, 143
- Soldi, S., et al. 2005, A&A, 444, 431
- Staubert, R., Koenig, M., Friedrich, S., Lamer, G., Sood, R. K., James, S. D., & Sharma, D. P. 1994, A&A, 288, 513
- Storchi-Bergmann, T., Eracleous, M., Ruiz, M. T., Livio, M., Wilson, A. S., & Filippenko, A. V. 1997, ApJ, 489, 87
- Storchi-Bergmann, T., Wilson, A. S., & Baldwin, J. A. 1992, ApJ, 396, 45
- Tadhunter, C. N., Packham, C., Axon, D. J., Jackson, N. J., Hough, J. H., Robinson, A., Young, S., & Sparks, W. 1999, ApJ, 512, L91
- Tadhunter, C. & Tsvetanov, Z. 1989, Nature, 341, 422
- Telesco, C. M., Piña, R. K., Hanna, K. T., Julian, J. A., Hon, D. B., & Kisko, T. M. 1998, Proc. SPIE, 3354, 534
- Terashima, Y., Iyomoto, N., Ho, L. C., & Ptak, A. F. 2002, ApJS, 139, 1
- Thompson, G. D., Levenson, N. A., Uddin, S. A., & Sirocky, M. M. 2009, ApJ, 697, 182
- Tingay, S. J., et al. 1998, AJ, 115, 960
- Tristram, K. R. W., et al. 2009, A&A, 502, 67
- Tristram, K. R. W., et al. 2007, A&A, 474, 837
- Turner, T. J., Perola, G. C., Fiore, F., Matt, G., George, I. M., Piro, L., & Bassani, L. 2000, ApJ, 531, 245
- Turner, T. J., George, I. M., Nandra, K., & Mushotzky, R. F. 1997, ApJS, 113, 23
- Urry, C. M. & Padovani, P. 1995, PASP, 107, 803
- Véron-Cetty, M.-P. & Véron, P. 2006, A&A, 455, 773
- Vignali, C., & Comastri, A. 2002, A&A, 381, 834
- Ward, M., Elvis, M., Fabbiano, G., Carleton, N. P., Willner, S. P., & Lawrence, A. 1987, ApJ, 315, 74
- Willick, J. A., Courteau, S., Faber, S. M., Burstein, D., Dekel, A., & Strauss, M. A. 1997, ApJS, 109, 333
- Wilson, A. S., Helfer, T. T., Haniff, C. A., & Ward, M. J. 1991, ApJ, 381, 79
- Yaqoob, T., et al. 2007, PASJ, 59, 283